Earth and Environmental Sciences

Environmental Chemistry

Catalysis of PAH biodegradation by humic acid shown in synchrotron infrared studies
Holman, H.-Y., K. Nieman, D.L. Sorensen, C.D. Miller, M.C. Martin, T. Borch, W.R. McKinney, R.C. Sims

Deciphering Ni sequestration in soil ferromagnanese nodules by combining x-ray fluorescence, absorption and diffraction at micrometer scales of resolution
Manceau, A., M.A. Marcus, N. Tamura, R.S. Celestre, A.A. MacDowell, R.E. Sublett, H.A. Padmore

Determining trace metal speciation in soils at molecular-scale by combined x-ray fluorescence, diffraction and absorption
Manceau, A., N. Tamura, R.S. Celestre, A.A. MacDowell, G. Sposito, H.A. Padmore

Development and evaluation of a new liquid cell system for soft x-ray absorption experiments
Matsuo, S., T. Kurisaki, H. Yamashige, P. Nachimuthu, R.C.C. Perera, H. Wakita

Investigation of interfacial chemistry of microorganisms
Ingram, J.C., D.E. Cummings, H.-Y. Holman, M.Downing

Microscale characterization of the location and association of TNT in soils
Ghosh, U., R.G. Luthy

Monitoring anthropogenic metal released in the environment via x-ray fluorescence, absorption and diffraction at micrometer scales of resolution
Manceau, A., M.A. Marcus, N. Tamura, R.S. Celestre, A.A. MacDowell, R.E. Sublett, H.A. Padmore, M. Kersten

New IR microscope and bench installed at BL 1.4
Martin, M.C., H.-Y. Holman, W.R. McKinney

O 1s XAS of H_2O in the solvation shell of monovalent and trivalent ions
Näslund, L.- Å., Ph. Wernet, H. Ogasawara, D. Edwards, S. Myneni, A. Nilsson

Spatial distribution of bacteria on basalt using SR-FTIR
Kauffman, M.E., H.-Y. Holman, R.M. Lehman, M.C. Martin

SR-FTIR study of bacteria-water interactions: Acid-base titration and silification experiments
Yee, N., L.G. Benning, M.J. Tobin, K.O. Konhauser

Surface spectroscopy of nano-scale reactions in aqueous solution
Pecher, K.H., B. Tonner

The use of micro-FTIR to characterize soil minerals and boron adsorption
Pittiglio, S., H.E. Doner

Valence-state imaging of mineral micro-intergrowths
Smith, A.D., P.F. Schofield, A. Scholl

Catalysis of PAH Biodegradation by Humic Acid Shown in Synchrotron Infrared Studies

Hoi-Ying N. Holman,[1] Karl Nieman,[2] Darwin L. Sorensen,[2] Charles D. Miller,[3] Michael C. Martin,[4] Thomas Borch,[5] Wayne R. McKinney,[4] and Ronald C. Sims[2]
[1]Center for Environmental Biotechnology, Lawrence Berkeley National Laboratory, Berkeley, CA 94720
[2]Utah Water Research Laboratory, Utah State University, Logan, UT 84321
[3]Biology Department, Utah State University, Logan, UT 84321
[4]Advanced Light Source Division, Lawrence Berkeley National Laboratory, Berkeley, CA 94720
[5]Center for Biofilm Engineering, Montana State University, Bozeman, MT 59717

INTRODUCTION

Humic acids (HAs) are complex organic molecules produced by the decomposition of plant and animal remains in soils. The surfactant-like micellar microstructure of HA is thought to accelerate the degradation of polycyclic aromatic hydrocarbons (PAHs) by enhancing PAH solubility, thereby increasing the PAH bioavailability to microorganisms. Despite abundant evidence that HA is important in the bioremediation of several anthropogenic pollutants, its role in the detoxification of PAHs by microbes remains uncertain.

Previous inconclusive results motivate a novel approach to the study of this important biogeochemical process. We used SR-FTIR spectromicroscopy to examine the effects of soil HA on biodegradation of the model PAH pyrene in the presence of a colony of Mycobacterium sp. JLS, on a mineral surface in an unsaturated environment. Infrared spectra measured during the onset and progress of biodegradation constitute the first microscopic study of this process to be made in real time.

PROCEDURE

SR-FTIR spectra were obtained at ALS BL1.4.3 from samples of M. sp. JLS as they degraded pyrene on magnetite surfaces, with and without the addition of Elliott Soil Humic Acid (ESHA). The pyrene-degrading microorganism M. sp. JLS is a gram-positive, rod-shape bacterium (GenBank accession no. AF387804); our samples were recently isolated from PAH-contaminated soil at the Libby Groundwater Superfund Site in Libby, Montana, USA. Our mineral substrates were freshly cleaved and sonicated surfaces of small chips (less than 1 cm in diameter) of magnetite rock from Minerals Unlimited of Ridgecrest, CA.

The time-dependent pyrene biodegradation experiments were began by adding 2.5 ml of cell suspension (~1.5 × 108 cells/milliliter) of M. sp. JLS onto the prepared magnetite chips. A custom IR microscope-stage mini-incubator was used to maintain the proper growth conditions for M. sp. JLS, while allowing *in situ* FTIR spectromicroscopy measurements. For abiotic controls, no M. sp. JLS was applied. Non-overlapping IR spectral markers were selected to monitor each component.

RESULTS

Figure 1 summarizes the time series of infrared spectra obtained by repeatedly measuring the same location on each pyrene-coated sample for more than a month. Since the sample surface is different for each experiment, the absolute value of absorbance can vary. However by monitoring the same position on each sample individually, the changes in absorption are quantitative. Over a similar period, the infrared spectra obtained from samples free of pyrene did not show statistically significant changes.

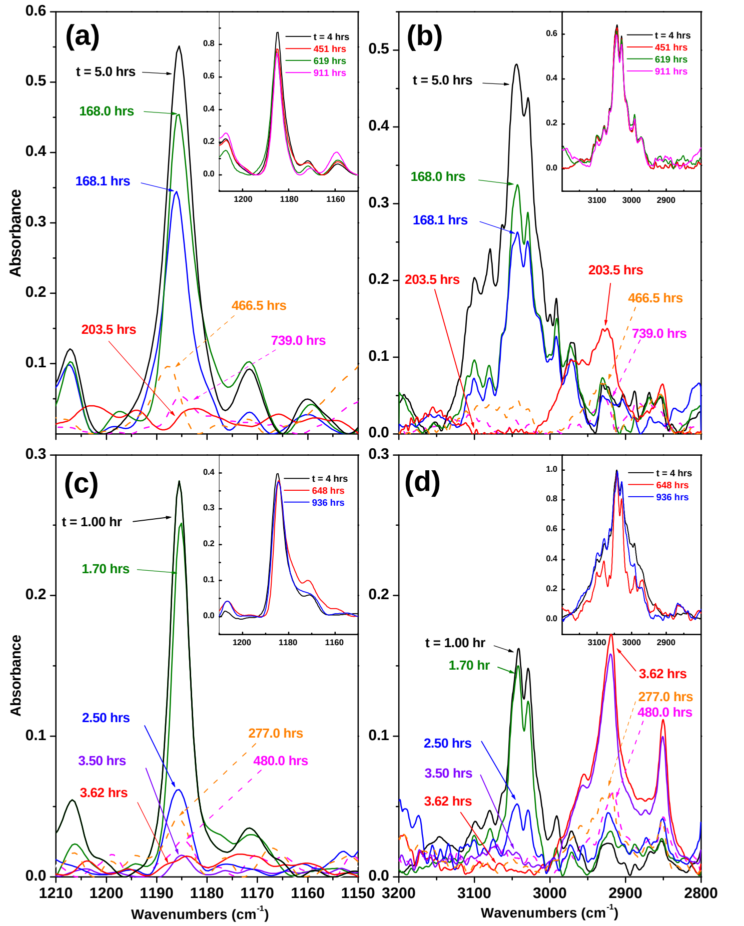

Figure 1. Time series of SR-FTIR absorption bands corresponding to pyrene and biomass formation following the degradation of pyrene by Mycobacterium sp. JLS on magnetite surfaces. Panels (a) and (b) are without ESHA; panels (c) and (d) are with ESHA. (a) and (c) show a pyrene absorption band at 1185 cm^{-1}. (b) and (d) show a pyrene doublet at 3044 and 3027 cm^{-1} and biomass IR absorption at 2921 and 2850 cm^{-1}. Inserts are abiotic control experiments.

For samples without ESHA, pyrene biodegradation starts very slowly, and about 168 hours elapse before significant changes are observed. Biodegradation then proceeds quickly, and all the observed pyrene is completely degraded within the next 35 hours. As the pyrene peaks in the spectra disappear, we observe an increase in the biomass IR absorption peaks, implying concurrent biomass formation during the consumption of pyrene (Fig. 1, panels (a) and (b)). By contrast, the biodegradation of pyrene on samples with ESHA begins almost immediately (~1 hour) after the introduction of M. sp. JLS (Fig. 1, panels (c) and (d)). The degradation of the observed pyrene is complete by the fourth hour. Again we detect an increase in biomass absorption during the later stage of the pyrene degradation, which implies that biomass formation is concurrent with the consumption of pyrene.

Figure 2 displays pyrene concentration and biomass versus time under three different conditions, as measured by associated spectral absorbances normalized to remove surface effects as described above. Abiotic results show that pyrene remains on the mineral surface, with only slow removal mechanisms. Pyrene degradation by M. sp. JLS without ESHA did not proceed until ~ 170 hours after the introduction of the bacteria, followed by a rapid decrease of pyrene and a rapid increase of biomass within the next thirty-five hours, as described earlier. After the pyrene was depleted the biomass signal significantly decreased, presumably as the M. sp. JLS bacteria transformed themselves into ultramicrocells, a starvation-survival strategy commonly observed among bacteria in oligotrophic environments. In the presence of ESHA, pyrene biodegradation begins within an hour and the observed pyrene is depleted by the end of the fourth hour, with a concurrent increase of biomass. It is likely that the water-insoluble pyrene is solubilized into cores of ESHA pseudo-micelles and therefore becomes available for bacterial consumption.

Over longer times, IR absorption bands of pyrene on magnetite surfaces showed a slight increase and decrease. The increase is probably due to pyrene diffusing from pyrene trapped in

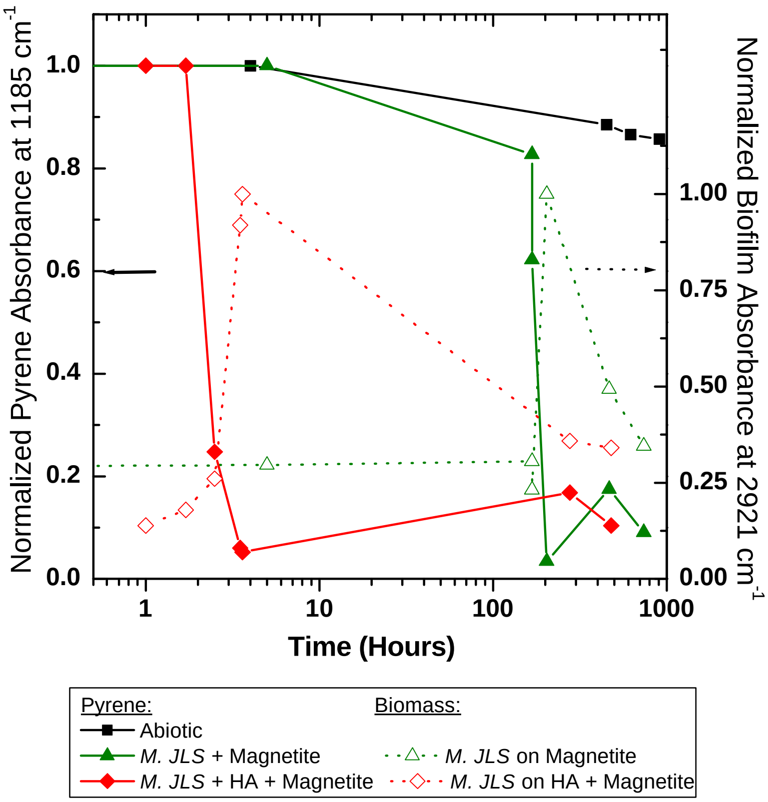

Figure 2. Summary of IR results showing that pyrene degradation occurs much faster when ESHA is present (note the log scale on the time axis). The color scheme is black for abiotic, green for biotic without ESHA, and red for biotic with ESHA. The solid lines correspond to pyrene and the dotted lines correspond to the biomass.

micropores of the magnetite and/or neighboring surfaces of higher pyrene concentration. Thus the first wave of rapid depletion of pyrene by M. sp. JLS set up a diffusion gradient from the pyrene-containing micropores toward the bacterial colony, leading to a subsequent small increase in pyrene concentration. For the surface containing ESHA, the biomass remained almost constant over a period of more than 200 hours, indicating that the flux of pyrene from the micropores was sufficient to maintain the bacterial colony. For the surface free of ESHA, there is little evidence of the presence of a quasi-steady state biomass.

DISCUSSION

Our results have significant implications for the bioremediation of contaminated soils. In many PAH-contaminated sites, bioremediation is specified by the U.S. Environmental Protection Agency as the preferred remedial technology. Bioremediation of PAH-contaminated soils is often limited, however, by the low solubility of PAH, which inhibits microbial uptake. Adding synthetic surfactants to enhance PAH solubility may be toxic to natural microorganisms and further inhibit bioremediation. Based on results reported here, a potential alternative in unsaturated soil environments may be the application of natural HA to accelerate the biodegradation of PAH.

SR-FTIR spectromicroscopy can assess real-time interactions between multiple constituents in contaminated soils. Combined with conventional mineralization measurements, which monitor respiration through carbon dioxide production, SR-FTIR spectromicroscopy is a powerful tool for evaluating bioremediation options and designing bioremediation strategies for contaminated vadose zone environments.

A longer version of this work will be published in Environmental Science and Technology, 2002.

This work was supported by the Director, Office of Energy Research, Office of Basic Energy Sciences, Materials Science Division, of the U.S. Department of Energy under Contract No. DE-AC03-76SF00098.

Principal investigator: Hoi-Ying N. Holman, Lawrence Berkeley National Laboratory. Email: hyholman@lbl.gov. Telephone: 510-486-5943.

Deciphering Ni sequestration in soil ferromanganese nodules by combining X-ray fluorescence, absorption and diffraction at micrometer scales of resolution

A. Manceau[1,2], M.A. Marcus[1], N. Tamura[1], R.S. Celestre[1], A.A. MacDowell[1], R.E. Sublett[1], H.A. Padmore[1]
[1]Advanced Light Source, Lawrence Berkeley National Laboratory, Berkeley, CA 94720
[2]Environmental Geochemistry Group, Hilgard Hall, University of California, Berkeley, CA 94720

Soils are a major sink for anthropogenic Ni, and its migration to living organisms is an environmental concern because of its suspected carcinogenicity when it is speciated as nickel sulfate or combinations of nickel sulfides and oxides, provoking lung and nasal cancers. The anthropogenic nickel sources are the metal processing operations, the combustion of coal and oil, and amendments by sewage sludge. The crystal chemistry of nickel in oxidized and silicated ores has been abundantly studied for economic reasons, and in these formations Ni is predominantly associated with phyllosilicates and the Fe oxyhydroxide, goethite (α-FeOOH). During its journey from the source to its resting place in soils, Ni can undergo many chemical transformations, and understanding how this element is naturally sequestered helps provide a solid scientific basis for maintaining soil quality and formulating educated strategies to remediate severely impacted areas. The most efficient and durable process responsible for trace metal sequestration in soils is the formation of ferromanganese micronodules, which often have been compared to the well-known oceanic Mn nodules. In this work, we have studied how nickel is sequestered in soil nodules from the Morvan region (France) by combining, for the first time, scanning X-ray microfluorescence (μSXRF), microdiffraction (μSXRD), and extended X-ray absorption fine structure (μEXAFS) spectroscopy, all applied at the micrometer-scale of resolution. The two first techniques were used to identify the host solid phase by mapping the distributions of elements and solid species, respectively. μEXAFS was then used to determine the mechanism of Ni binding by the host phase at the molecular scale. We showed that nickel substitutes for Mn^{3+} in the manganese layer of the MnO_2-$Al(OH)_3$ mixed-layer oxide lithiophorite. The affinity of Ni for this mineral was subsequently found to be characteristic of micronodules sampled from soils across the USA and Europe. Since many natural and synthetic materials are heterogeneous at nanometer to micrometer scales, the unprecedented synergistic use of μSXRF, μSXRD, and μEXAFS is expected to have broad applications to earth and materials science.

RESULTS AND INTERPRETATION

With μSXRF (three first maps) the distribution of Fe, Mn, and Ni were first determined, and it was found that Mn and Ni were systematically associated in the six different soil nodules examined in this study. Then, mineral abundance maps were produced by integrating at each point-of-analysis the diffracted intensities of the non-overlapping (020) and (200) reflections at ~4.45 Å and ~2.57 Å for phyllosilicate, the (101) and (301) reflections at 4.19 Å and 2.69 Å for goethite, the (001) reflection at 7.1-7.2 Å for birnessite, and the (001) and (002) reflections at 9.39 Å and 4.69 Å for lithiophorite. The reliability of this quantitative treatment was verified by comparing mineral maps calculated using independent (*hkl*) reflections of the same mineral species. The distribution of Fe-vernadite, a common soil mineral, was not mapped because it was systematically detected throughout the examined nodules without significant gradient of concentration. This Fe-Mn disordered phase (also termed Mn-feroxyhite), that is dispersed throughout the nodule matrix filling pores and aggregating coarse grains, acts as a cementing agent for the nodules.

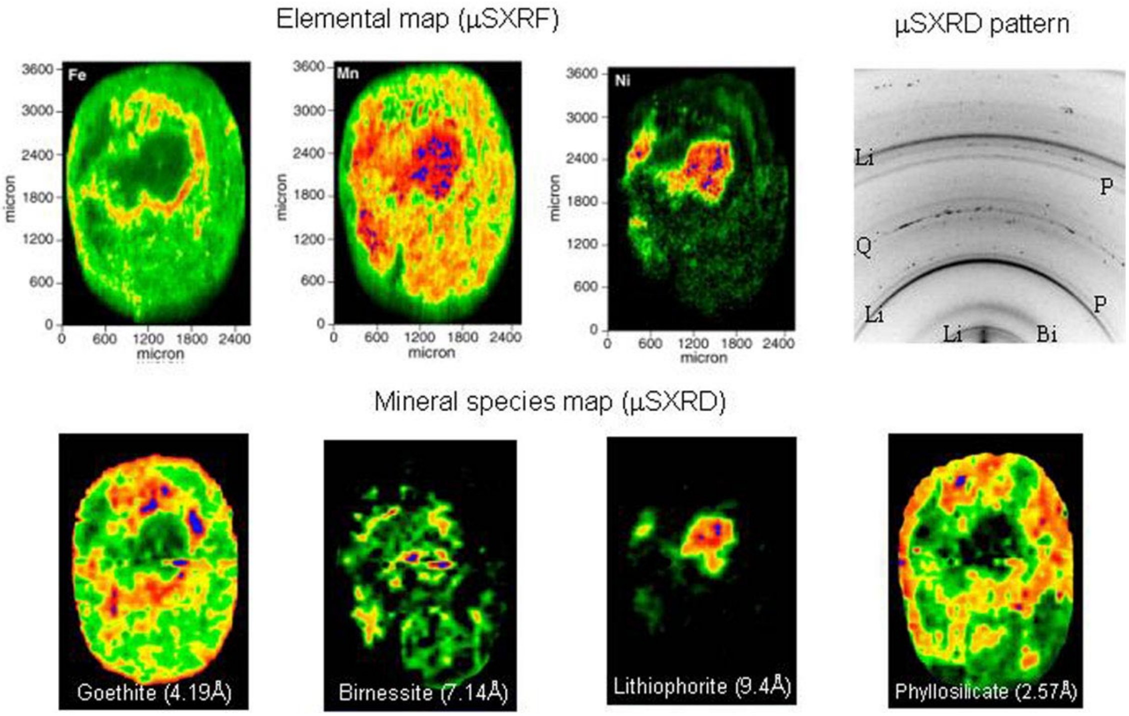

Figure 1. Combined fluorescence - diffraction measurements recorded at Beamline 7.3.3. on a ferromanganese soil nodule. The three images on the top are elemental maps obtained by µSXRF, and the four images on the bottom are mineral species maps obtained by integrating at each point of analysis the intensities of the relevant (*hkl*) reflections along the Debye rings of the two-dimensional XRD patterns (d-spacings are indicated in parenthesis). One XRD pattern is presented to the top right. Li = lithiophorite, Bi = birnessite, P = phyllosilicate, Q = quartz.

The comparison of the µSXRF and µSXRD maps clearly shows that nickel and lithiophorite have the same contour maps, therefore suggesting that Ni is bound to this particular mineral phase. The systematic association of Ni-lithiophorite suggests that Ni should be located in a definite cation site of the manganese oxide crystal structure. To determine the Ni site, Ni K-edge µEXAFS spectra were collected on Beamline 10.3.2. in Ni 'hot spots' from several nodules. All spectra were identical, indicating that the incorporation mechanism of nickel is unique, and is the key to understanding its sequestration in soils. Qualitative information about the local structure of Ni can be obtained by comparing the unknown µEXAFS spectrum to reference EXAFS spectra from relevant model compounds. As expected from µSXRF – µSXRD experiments, the two reference spectra for Ni in goethite and phyllosilicate did not match the unknown spectrum, confirming that Ni is not sequestered in these forms (data not shown). Differences in frequency and shape of the EXAFS oscillations were also observed with birnessite, in which Ni is sorbed above vacant Mn sites, and with lithiophorite, in which Ni is located within the gibbsitic Al layer (Fig. 2a). The radial structure functions (RSFs) obtained by Fourier transforming EXAFS spectra for the reference and the soil lithiophorite both exhibit, after the first oxygen peak, a second peak at roughly $R + \Delta R = 2.6$ Å, that is at a distance characteristic of edge-sharing linkage between metal octahedra (Fig. 2b). This result alone suggests that Ni is located within one of the two octahedral layers of the lithiophorite structure. To solve this alternative, suffice it to examine the phase of the imaginary part of the Fourier transform, because waves backscattered by Al and Mn atoms are almost out-of-phase. Examination of Fig. 2c shows that the unknown and lithiophorite reference have their electronic waves shifted by $\sim\pi$ in the 2.2 – 3.1 Å $R + \Delta R$ interval, thus indicating that Ni is substituted for Mn in the soil lithiophorite. In keeping with this conclusion, the two waves are logically in phase in the 1.0 – 2.2 Å R + ΔR interval, since in both structures Ni is octahedrally coordinated to oxygen atoms.

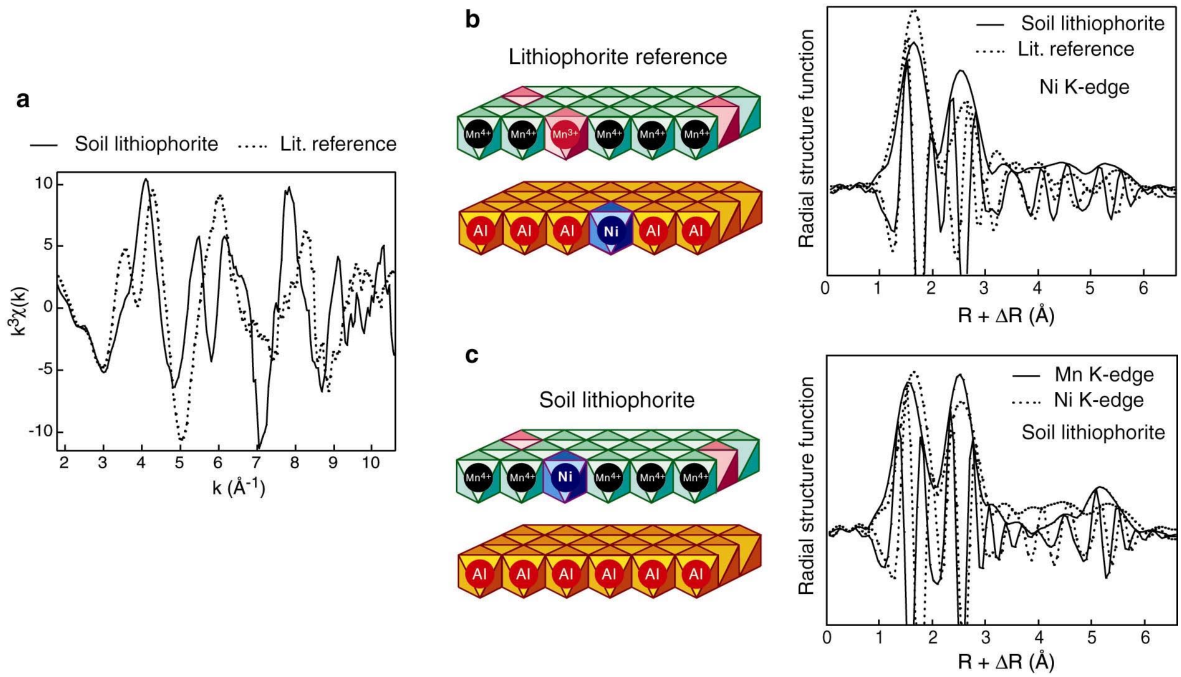

Figure 2. Ni K-edge μEXAFS spectrum (**a**) and Fourier transform (modulus plus imaginary part) (**b,c**) from a 'hot spot' of the core of the nodule, compared to the Ni- and Mn-edge data from a Ni-containing lithiophorite reference, in which Ni substitutes for Li in the $Al(OH)_3$ layer. Data were collected on Beamline 10.3.2.

Since Ni^{2+} has an effective radii 30% greater than Mn^{4+}, one may wonder how the Ni-Mn substitution is realized. To answer this question, Ni- and Mn-RSFs were plotted together (Figure 2b, bottom right), and the Ni- and Mn-EXAFS interatomic distances compared. A distinct feature in the Ni-RSF is the shift to higher R + ΔR values of the Ni-O peak, indicative of a relaxation of the Ni site owing to the larger ion size of the Ni^{2+} impurity (r = 0.69 Å) relative to Mn^{4+} (r = 0.53 Å) and Mn^{3+} (r = 0.645 Å). Since Ni^{2+} and Mn^{3+} have a size mismatch of only 7%, nickel likely substitutes on the trivalent manganese site. Likewise, the Al^{3+} site of the gibbsitic layer is clearly too small (r = 0.535 Å) to accommodate Ni^{2+}, and the larger Li^+ site (r = 0.76 Å) is probably energetically less favorable. This assumption is supported by recent atomistic calculations and EXAFS measurements on lanthanide-doped perovskite, which showed that the rare earth is energetically stabilized in smaller crystallographic sites. A best fit to our data was given by octahedral coordination of nickel with oxygen at 2.05 Å and six manganese at 2.91 Å, and average Mn-O and Mn-Mn distances of 1.92 Å and 2.92 Å, respectively. There was no indication of Ni-Ni pairs, for which Ni-Ni distances of 3.03 Å to 3.12 Å would be predicted. This result indicates that nickel did not precipitate as a hydroxide, hence confirming that the next-nearest coordination shell of Ni is made of Mn atoms. Similar results were obtained on nodules from flood plain soils in the USA, which suggests that the Ni species identified herein may correspond to a major sequestration form of Ni in Earth near-surface environments.

This work was supported by the LBNL Laboratory Director's Research and Development Fund and by the US Department of Energy, Office of Basic Energy Sciences, under contract # DOE-AC03-765F00098.

Principal investigator: Alain Manceau, Advanced Light Source, Ernest Orlando Lawrence Berkeley National Laboratory. Email: acmanceau@lbl.gov. Telephone: 510-643-2324.

Determining trace metal speciation in soils at molecular-scale by combined X-ray fluorescence, diffraction and absorption

A. Manceau[1,2], N. Tamura[1], R.S. Celestre[1], A.A. MacDowell[1], G. Sposito[2], H.A. Padmore[1]
[1] Advanced Light Source, Lawrence Berkeley National Laboratory, Berkeley, California 94720, USA
[2] ***Environmental Geochemistry Group, Hilgard Hall, University of California, Berkeley, CA 94720, USA***

INTRODUCTION

Understanding how environmentally-important trace metals are sequestered in soils at the molecular scale is critical to developing a solid scientific basis for maintaining soil quality and formulating effective strategies to remediate severely contaminated areas. The speciation of Zn and Ni in flood plain soils was determined by a novel synergistic use of three non-invasive synchrotron-based techniques, X-ray microfluorescence (µSXRF); X-ray microdiffraction (µXRD); and extended X-ray absorption fine structure spectroscopy (EXAFS). Eight nodules from the Mississippi basin were examined by µSXRF and µXRD on the 7.3.3. microdiffraction beamline, and complementary EXAFS measurements were performed at the European Synchrotron Radiation Facility in Grenoble (France). Here, only the first set of results is presented.

RESULTS AND INTERPRETATION

The chemical composition of the nodules was determined using inductively coupled plasma atomic emission spectroscopy (ICP-AES) and inductively coupled plasma mass spectroscopy (ICP-MS). These analyses gave [Fe] = 57526 (σ = 21213), [Mn] = 25592 (σ = 17716), [Zn] = 76 (σ = 51), [Ni] = 67 (σ = 21) mg/kg. The σ variability of the bulk analyses is relatively low, and contrasts with the µSXRF maps, which show that individual nodules are highly heterogeneous at the micrometer scale, containing distinct areas of concentrated Fe, Mn, Ni and Zn (Fig. 1).

The mineralogy and crystal chemistry of Zn and Ni in the series of nodules is completely represented by the three samples in Fig. 1. Nodule 1 shows, on average, little correlation between Fe and Mn ($r_{Fe\text{-}Mn}$= 0.62), but visual inspection of the maps shows that the degree of correlation varies laterally. The richest Fe areas in the outer region are strongly depleted in Mn, whereas the inner region contains areas of both high Mn and high Fe. Zn and Ni are strongly correlated with Fe ($r_{Fe\text{-}Zn}$ = 0.84, $r_{Fe\text{-}Ni}$ = 0.88) and, to a lesser extent, with Mn ($r_{Mn\text{-}Zn}$ = 0.71, $r_{Mn\text{-}Ni}$ = 0.78). The relatively high $r_{Mn\text{-}Ni}$ value does not necessarily indicate that a Ni fraction is actually associated with Mn, but instead can result from the incomplete separation of Fe and Mn in the core of a nodule. µXRD patterns were collected with a CCD camera at different points selected on the elemental maps. The outermost Fe-rich region was found to consist of finely-dispersed goethite (α–FeOOH). Quartz, feldspar, titanium oxide, and carbonate grains also were detected. The Fe-Mn core consists of either Mn-feroxyhite (δ-FEOOH) or Fe-vernadite (δ-MnO_2), depending on the Fe/Mn ratio. Therefore, Zn and Ni appear to be predominantly bound to goethite in this nodule.

Mn, Fe, Zn, and Ni were also unevenly distributed in nodule 2 (Fig. 1b), which showed a moderate overall correlation between Fe and Mn ($r_{Fe\text{-}Mn}$ = 0.78). However, the central region is high in Fe and Mn, whereas the external Fe layer is depleted in Mn. As with the previous nodule, this result illustrates the spurious meaning of elemental correlations calculated solely from total chemical analyses. Nodule 2 possesses a Zn-Ni "hot spot", about 80 x 80 μm^2 in area, which is strongly

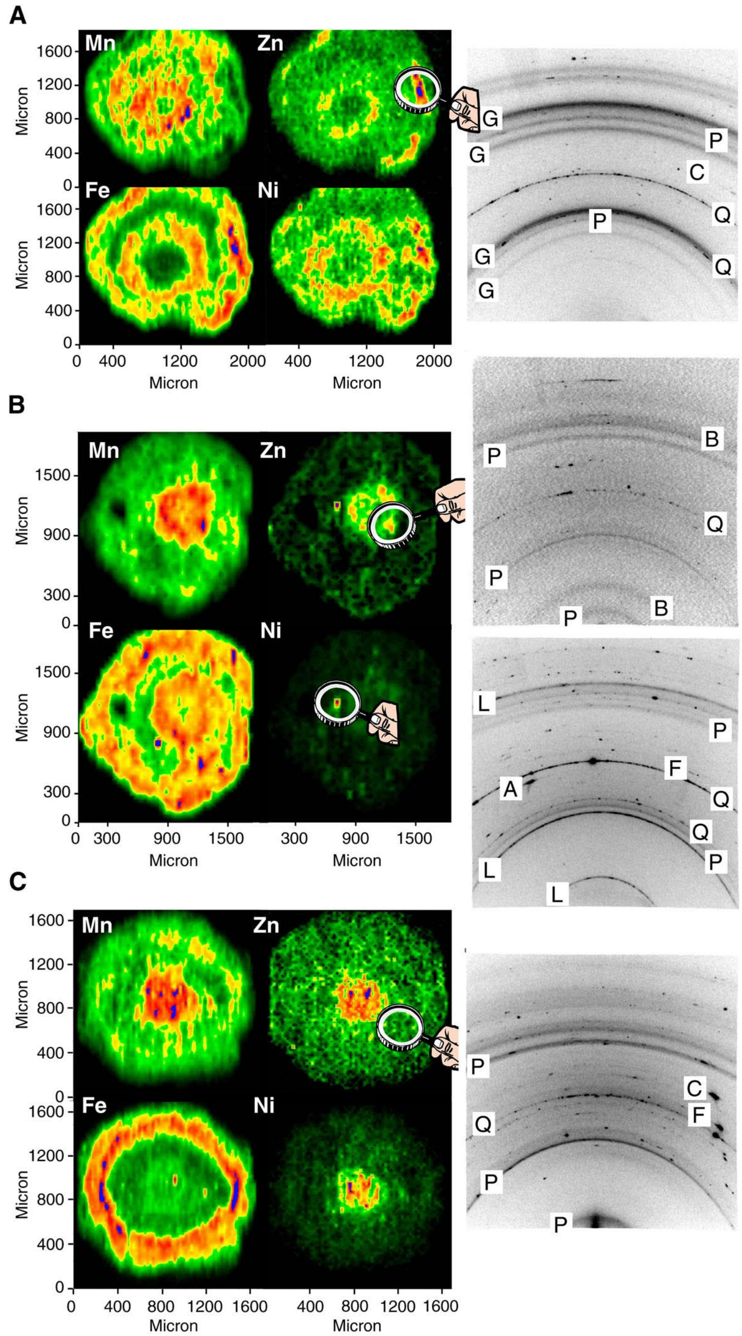

Figure 1. Synchrotron-based micro-X-ray fluorescence (µSXRF) maps obtained by scanning soil nodules under a monochromatic beam (E = 10 keV; beam size on the sample: 10 µm H x 25 µm V; step size: 32 x 32 µm (a), 42 x 42 µm (b), 25 x 25 µm (c); counting time: 5 to 8 s/point). µXRD patterns were collected at selected points of interest using a 1024 x 1024 pixels CCD camera and an exposure time of 10 to 20 min (E= 6.0 keV (a, b) and 6.3 keV (c)). All data were collected in reflection geometry mode by inclining the sample at 6° θ. B = hexagonal birnessite (main diffraction peaks at 7.1-7.2 Å, 2.45 Å, and 1.41 Å), G = goethite (main diffraction peaks at 4.18 Å and 2.69 Å), L = lithiophorite (main diffraction peaks at 9.4 Å, 4.7 Å, and 2.37 Å), P = phyllosilicate (main diffraction peaks at 4.45-4.48 Å, 2.55–2.58 Å, and 1.50 Å). In (a) Ni and Zn are associated with goethite (α-FeOOH); in (b) Ni is associated with lithiophorite, and Zn with lithiophorite and birnessite; in (c) Ni is associated with lithiophorite and Zn with lithiophorite and phyllosilicate.

correlated with Mn. The core of the nodule is enriched in Zn as well, but devoid of Ni, suggesting that nodule 2 contains two major Zn species, but only a single Ni species, one which also contains Zn. The mineralogical nature of the minute Mn grain containing both Zn and Ni was identified by µXRD as lithiophorite, a MnO_2 - $Al(OH)_3$ mixed-layer phyllomanganate (Fig. 2). In the two-dimensional XRD pattern, Bragg reflections from this grain formed a continuous Debye ring, characteristic of a powder diffraction pattern. The lithiophorite is, therefore, very fine-grained like most natural reactive particles. Randomly-layered birnessite (also termed vernadite), together with phyllosilicate, was positively identified in the central region by µXRD (Fig. 1b). Vernadite and lithiophorite are considered to be the two predominant Mn mineral species in near-surface environments, but their defective structure (vernadite) and small particle size pose major problems for identifying them by conventional XRD. The combination of µSXRF and µXRD provides the necessary lateral resolution for establishing their presence and role in the sequestration of trace metals.

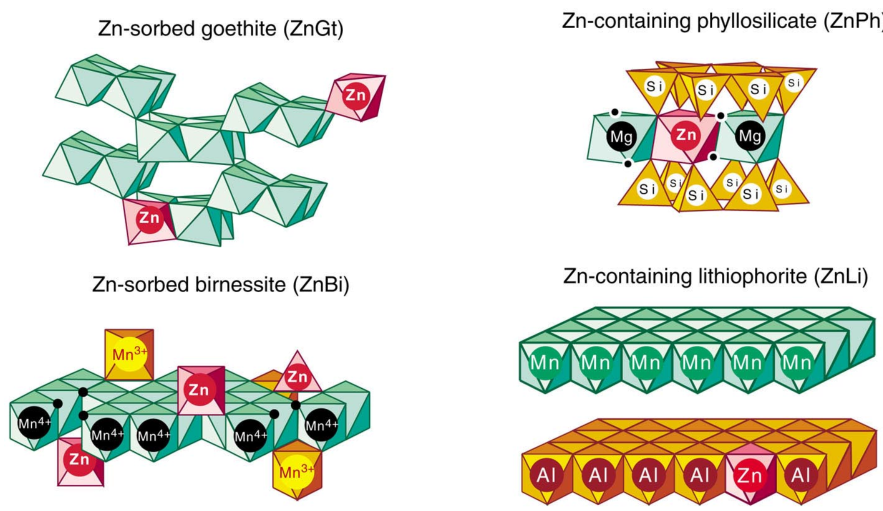

Figure 2. Structure of minerals in which Zn and Ni are sequestered.

Two Zn fractions were also detected in nodule 3 (Fig. 1c). In the first, Zn is concentrated with Ni and Mn at the core, which, according to µXRD, contains lithiophorite and phyllosilicate, a geochemical association already found in nodule 2. The second fraction of Zn has a uniform background signal distributed throughout the nodule and likely as well in the central region, where it is masked by the Zn,Ni lithiophorite species. Clearly, this second Zn fraction is not bound either to Fe or Mn oxides, because neither the Fe nor the Mn map shows areal contours similar to the Zn map. µXRD patterns collected in Zn-containing (but Fe- and Mn-depleted) regions showed the presence of dioctahedral phyllosilicates (Fig. 1c). Therefore, the second Zn fraction likely corresponds to a Zn-containing phyllosilicate. It was almost impossible to find regions containing only Fe or Mn oxides. For example, the four two-dimensional µXRD patterns presented in Fig. 1 all contain diffraction rings at 4.45-4.48 Å and 2.55-2.58 Å, typical of the 020-110 and 130-200 reflections that characterize sheet silicates. A peak at 1.50 Å was observed systematically at higher diffraction angles, thus indicating the mostly dioctahedral structure of these minerals. Elemental correlation coefficients for nodule 3 can be interpreted readily based on these results. Little correlation was obtained for Fe and Mn ($r_{Fe\text{-}Mn}$=0.69), in agreement with the nonoverlapping contour maps for these two elements. The Mn-Zn correlation is moderate ($r_{Mn\text{-}Zn}$=0.76) owing to the partial association of Zn with phyllosilicate, whereas the Mn-Ni correlation is strong (r_{Mn-Ni}=0.82) since Ni is uniquely bound to lithiophorite. Correlations between Fe and Zn (r_{Fe-Zn}=0.44) or Fe- and Ni (r_{Fe-Ni}=0.33) are low, as expected.

In summary, µSXRF and µXRD microanalyses showed that Zn is bound to four mineral species, goethite, phyllosilicate, hexagonal birnessite, and lithiophorite, whereas nickel is sequestered by goethite and lithiophorite. This difference in speciation of Zn and Ni provides a clue to the observed higher partitioning of Ni in the soil nodules over the soil matrix. Nodules commonly form in soils with restricted internal drainage by the solubilisation of Fe(II) and Mn(II) under reducing conditions, followed by precipitation as Fe(III) and Mn(III,IV) oxides under oxidising conditions. Consequently, concretions have the same quantities of phyllosilicates and coarse grains (quartz, feldspar, titanium oxides…) as does the soil matrix, but they contain a higher quantity of finely-divided Fe and Mn oxides that cement soil material together and reduce its porosity. Since Zn is predominantly speciated as a phyllosilicate (EXAFS data not shown), and because this latter mineral is uniformly present in the soil, Zn partitioning in nodules is necessarily limited. The high Ni partitioning into the nodules results directly from selective sequestration by Fe and Mn oxides, the principal minerals that cause nodule formation. Thus, the novel combination of µSXRF, µXRD, and EXAFS spectroscopy provides the approach needed to speciate metals in a natural matrix not possible to study accurately with conventional techniques.

This work was supported by the LBNL Laboratory Director's Research and Development Fund and by the US Department of Energy, Office of Basic Energy Sciences, under contract # DOE-AC03-765F00098.

Principal investigator: Alain Manceau, Advanced Light Source, Ernest Orlando Lawrence Berkeley National Laboratory. Email: acmanceau@lbl.gov. Telephone: 510-643-2324.

Development and Evaluation of a New Liquid Cell System for Soft X-Ray Absorption Experiments

S. Matsuo[1], T. Kurisaki[2], H. Yamashige[2], P. Nachimuthu[3], R. C. C. Perera[4], and H. Wakita[1,2]
[1]Advanced Materials Institute, Fukuoka University, Nanakuma, Jonan-ku, Fukuoka 814-0180, Japan
[2]Department of Chemistry, Faculty of Science, Fukuoka University, Nanakuma, Jonan-ku, Fukuoka 814-0180, Japan
[3]Department of Chemistry, University of Nevada Las Vegas, Las Vegas, NV 89154-4003, USA
[4]Center for X-ray Optics, Lawrence Berkeley National Laboratory, Berkeley, CA 94720, USA

INTRODUCTION

Soft X-ray is well used as a means available to investigate the electron state of valence band in a material, because the energy of soft X-ray is close to that of the valence band and strongly affects the material in the electronic state. The soft X-ray absorption spectrum provides information on the electron states between the absorbing atom and neighboring atom(s) in a material, in addition, the researches by the soft X-ray absorption spectroscopy are extensively developed with the increase of the number of the target atoms for the researches, because the elements absorbing the soft X-ray include not only the light elements, but also the elements which can cause the L- and M-shells excitation. So far, for solid samples, the soft X-ray absorption spectroscopy has been utilized for the studies of developments for functional materials, the speciation of pollution compounds, the mechanistic analysis of catalytic reactions and vital functions [1]. However, for the soft X-ray absorption experiments for liquid samples, it has really been difficult to design the liquid cell system which is able to measure the absorption spectra under atmospheric pressure. In this paper, we report on a new liquid cell system for the soft X-ray absorption experiments developed at ALS, and show the X-ray absorption near-edge structure (XANES) spectra for aqueous Al salt solutions by the use of the cell system.

APPARATUS

The setup of the developed cell system is depicted in Figure 1. This cell system has been installed in BL6.3.1, and has the vacuum system with two shutters to keep the pressure in the path, ca. 10^{-7} Torr. The window attached the silicon nitride (Si_3N_4) membrane, which has 150 nm in thickness and 1 mm square, is fixed on the end of the pressure path. A liquid sample is trapped between two other Si_3N_4 membrane windows, on which the polystyrene microspheres (ca. 10 μm in diameter) are dropped in advance. The liquid sample trapped is fixed on the sample holder, which is made of stainless steel and designed as the beam is transmitted by the sample liquid and detected by the silicon photodiode under the optimal condition, and then it is put on the sample stage. The end of the pressure path, sample stage, and detector are covered with the acryl case.

EXPERIMENTAL

Aluminum K-edge XANES spectra were collected by a transmission mode using the cell system for aqueous solution samples and by a total electron yield method for powder samples pressed onto the conductive carbon tape. The measured aluminum compounds were aluminum chloride ($AlCl_3$), aluminum nitrate nonahydrate ($Al(NO_3)_3 \cdot 9H_2O$), sodium aluminate, and aluminum ethylenediaminetetraacetate (Al-EDTA) complex. The aqueous solution of Al-EDTA was

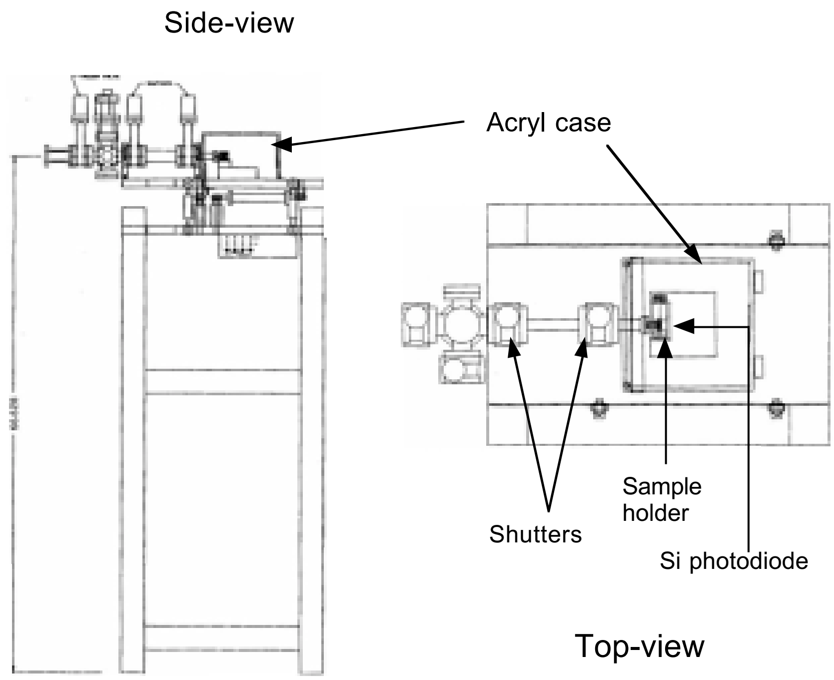

Figure 1. Setup of the XAFS cell system of soft X-ray absorption spectral measurements for solution samples.

prepared by adding 0.5 M $Al(NO_3)_3·9H_2O$ aqueous solution (25 ml) to 0.5 M EDTA tripotassium salt aqueous solution (25 ml) and finally adjusted to pH 4.5. The other solution samples were high-concentrated aqueous solutions. Al-EDTA sodium salt dihydrate was purchased from DOJINDO Laboratories. Data were collected from 1550 to 1620 eV at intervals of 0.2 eV with the speed of 0.5 s a point. In the measurements, Helium gas was made to flow and to fill in the acryl case, which was covered with a black cloth.

RESULTS

The Al K-edge XANES spectra for the aqueous solutions of $AlCl_3$, $Al(NO_3)_3·9H_2O$, sodium aluminate, and Al-EDTA are shown in Figure 2 with those for their powder samples. In the powder samples, all the peak tops of the XANES spectra appear in almost similar energy position. In the aqueous solution samples, on the other hand, the peak tops of the XANES spectra of $AlCl_3$ and $Al(NO_3)_3·9H_2O$ are similar in the position to those in their powder samples, while those of sodium aluminate and Al-EDTA are different from those in their powder samples, and shift to the low energy side. These results indicate that the coordination numbers for $AlCl_3$ and $Al(NO_3)_3·9H_2O$ little change between the powder and aqueous solution samples, and those for sodium aluminate and Al-EDTA show a change. In fact, by the NMR study the coordination number of Al-EDTA has

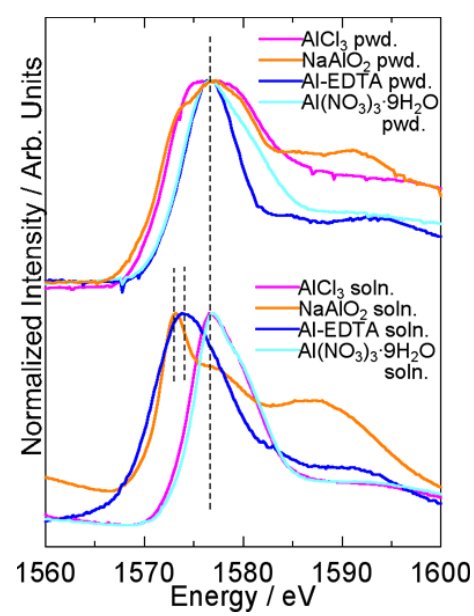

Figure 2. Al K-edge XANES spectra of powders and aqueous solution of various Al compounds.

been proposed to be six in powder and five in aqueous solution [2]. Accordingly, the peak position of the XANES spectra for Al-EDTA can be related with the coordination number. Furthermore, the relation between the peak position and coordination number would be also applied for all aluminum compounds.

CONCLUSION

The new liquid cell system for the soft X-ray absorption experiments developed at ALS enables us to record the spectra characteristic of chemical species in solution. For the XANES spectra of aqueous aluminum salt solutions obtained by the liquid cell system, the change of the peak position was related with the coordination structure, especially coordination number.

REFERENCES

1. H. Wakita, Bunseki (in Japanese) **1**, 24 (2002).
2. T. Yokoyama, Y. Tsuji, T. Kurisaki, and H. Wakita, presented at the IUPAC International Congress on Analytical Sciences 2001, Waseda University, Tokyo, Japan, 2001 (unpublished).

This work was supported by the Advanced Materials Institute, Fukuoka University and by the Director, Office of Energy Research, Office of Basic Energy Sciences, Materials Science Division, of the U.S. Department of Energy under Contract No. DE-AC03-76SF00098.

Principal investigator: Hisanobu Wakita, Advanced Materials Institute and Department of Chemistry, Faculty of Science, Fukuoka University. Email: wakita@fukuoka-u.ac.jp. Telephone: +81-92-801-8883.

Investigation of Interfacial Chemistry of Microorganisms

Jani C. Ingram,[1] David E. Cummings,[1] Hoi-Ying Holman,[2] and Matthew Downing[3]
[1]Idaho National Energy and Environmental Laboratory, ID
[2]Lawrence Berkeley National Laboratory, CA
[3]Shawnee High School, NJ

INTRODUCTION

Remediation of Department of Energy (DOE) sites contaminated with toxic metals and radionuclides is a complex and costly problem. Several bioremediation strategies currently being explored exploit the metabolism of naturally-occurring dissimilatory metal-reducing bacteria (DMRB). These bacteria catalyze the mobilization of some metal oxide-associated trace elements and the precipitation of many otherwise soluble metals and radionuclides. Our recent work centers on the effects of co-contaminating trace metals on the microbe-mineral interface.

RESULTS

Secondary ion mass spectrometry (SIMS) and synchrotron radiation Fourier transform infrared spectroscopy (SR-FTIR) were applied to examine biochemical changes incurred at the surface of Shewanella putrefaciens cells due to exposure to soluble arsenic. Cells responded to the insult with altered membrane fatty acids (observed by SIMS) and exopolysaccharide production (observed by SR-FTIR).

SR-FTIR at ALS beamline 1.4.3 was used to analyze *S. putrefaciens* cells with and without exposure to 100 mM As(V). The main difference between the spectra of stationary phase cells was the clear lack of a broad peak associated with carbohydrates in the As-exposed cells that was present in the unexposed cells (Figure below). In its place were two distinct peaks indicative of phosphodiester bonds. Phosphodiester bonds are abundant in cell membranes, forming the junction between glycerol and fatty acids. Cell surface carbohydrates likely indicate either a capsule (exopolysaccharides), or common membrane lipids called lipopolysaccharides (LPS). The role of the capsule is especially important in nature, where it can aid the cell in its defense against viruses, hydrophobic toxins such as detergents, and dessication. In addition, it has been implicated in the attachment of some microorganisms to solid substrates. An impaired ability to form exopolysaccharides would likely limit the cells competitive fitness in nature. The LPS may be largely responsible for the net negative charge on the cell surface, implicated in attachment, metal binding, and nutrient transport across the outer membrane. Additionally, the LPS may stabilize the membrane's physical shape and structure. An impaired LPS would also put the cells at a disadvantage in the environment.

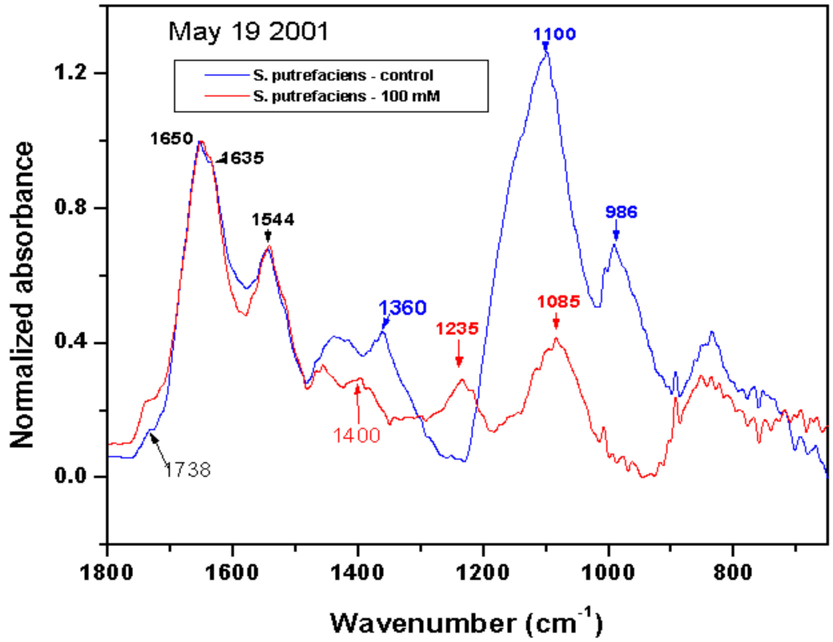

This work was supported by Idaho National Engineering and Environmental Laboratory.

Principal investigator: Jani C. Ingram, Idaho National Engineering & Environmental Laboratory (INEEL), Phone: (208) 526-0739, Fax: (208) 526-8541, email: uoa@inel.gov

Microscale Characterization of the Location and Association of TNT in Soils

U. Ghosh and R.G. Luthy
Department of Civil and Environmental Engineering, Stanford University, Stanford, CA 94305-4020

INTRODUCTION:

Numerous ammunition manufacturing facilities and ammunition testing sites across the world are faced with environmental problems associated with soils contaminated with trinitrotoluene (TNT) and other nitroaromatic compounds. Although a number of TNT treatment technologies have been developed recently [1,2], these techniques do not result in a high degree of mineralization of the explosive compounds present. Thus, a significant part of the contaminant mass remains in the soil as residues of the original contamination. The acceptance of cost-effective treatment techniques depends on better understanding of the stabilization of TNT and its nitroaromatic transformation products in soil. The chemical and biological availability of TNT residues in soil is determined primarily by the physical and chemical form in which TNT remain in soils. Reduction of TNT produces aminonitrotoluenes, which may covalently bond irreversibly with quinones, and reversibly with hydroquinones. Such transformation of molecular structure is implicated in making TNT transformation products unavailable for further degradation [3]. However, TNT residue may also be present in a solid form in soils, especially at former production facilities. Solid TNT particles may create a toxic zone in the vicinity thereby making biodegradation difficult. Thus it is important to understand the microscale nature of TNT residues found in contaminated soils.

In our previous work, microscale analytic techniques were used successfully to demonstrate the preferential binding of polycyclic aromatic hydrocarbons (PAHs) on coal-derived particles in sediment [4,5]. We showed in that work that PAH sorption on coal-derived particles is associated with minimal biodegradation, slow release rates, and high desorption activation energies, while PAH sorption on clay/silt particles is associated with significant potential biodegradability, relatively fast release rates, and lower desorption activation energies.

The primary focus of the current work is to develop microscale analytic techniques to assess whether crystalline TNT may exist in impacted soils and to apply these techniques to determine whether the presence of crystalline or pure TNT in soil may explain differences in biotreatability of TNT-impacted soils from the field.

RESULTS AND DISCUSSION:

The focus of this research is to develop methods to permit the identification at the particle and sub-particle scale whether solid-phase, crystalline TNT, or crystalline TNT transformation products exists in field soils. Infrared spectromicroscopy available at beamline 1.4 was used to detect the presence of solid TNT in contaminated soils. Although the fate of TNT and its transformation products in soil has been the subject of numerous investigations, important questions remain on whether pure solid TNT may account for an untreatable fraction of TNT in field samples. The hypothesis is that crystalline or pure TNT is toxic to microorganisms and not easily biotreatable and that differences in biotreatment of TNT-impacted soil may depend on whether the TNT is present as sorbed versus solid, crystalline form. Soil samples were obtained from two ammunition manufacturing facilities. Soils from these field sites are currently being tested for possible application of biotreatment technologies. Half a gram of each soil was spread on red clay mounted on a microscope slide. IR analysis was carried out in the reflectance mode. In our investigations using IR spectromicroscopy we observed the presence of significant quantities of residual crystalline TNT embedded in both soil samples. We could identify solid TNT based on the unique spectral characteristics of the nitro groups present in TNT. As shown in Figure 1, strong IR absorbance peaks near 1550 and 1350 wavenumbers are indicative of the asymmetric and symmetric stretch vibrations of the NO_2 groups present in the TNT molecules. To illustrate the physical location and form of the solid TNT particles, a representative soil agglomerate containing solid TNT was investigated for TNT presence using line scanning as shown in Figure 2. Multiple spots along a straight line through the TNT spot were analyzed in the IR spectromicroscope. As shown in Figure 2, the two absorbance peaks for the nitro groups show up when the scan passes through the TNT spot in the image shown on top. The rest of the soil barely shows any appreciable TNT signal. Thus, the residual TNT seems to be present predominantly in the solid particulate form. A light-microscope image of the solid TNT spot reveals a crystalline structure as shown in Figure 2. A unique finding in our work using IR spectromicroscopy is the direct measurement of residual crystalline TNT embedded in soil as opposed to TNT sorbed on mineral or organic matter. This finding of the microscale nature of TNT residuals in field materials has a major implication on its availability and toxicity. Current work in this research is investigating the effect of crystalline TNT on biological and chemical treatment methods. We are investigating the behavior of TNT degrading organisms near the vicinity of TNT crystals in soil using live-dead staining procedures and visualization through laser confocal microscopy. Results from this research will provide important information on the particle and sub-particle locations of solid, crystalline TNT and whether this accounts for the variability in biotreatment of TNT.

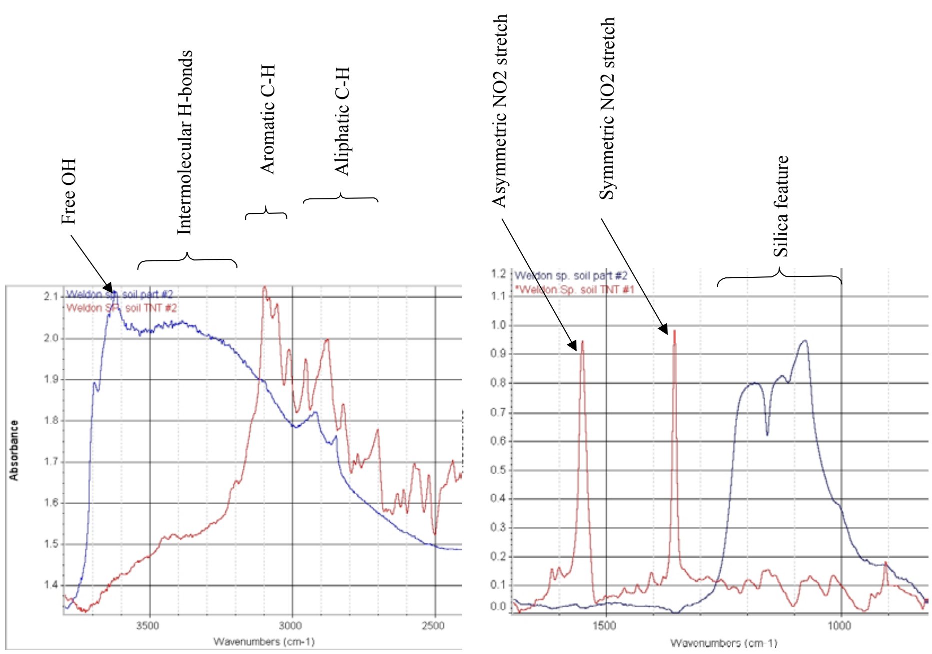

Figure 1. Results of experiments conducted at Beamline 1.4.2 illustrating the use of IR spectromicroscopy to identify the location of TNT micro-crystals present in contaminated soil from an ammunition manufacturing facility. The red line shows the absorbance spectra of the TNT crystals, and the blue line shows the absorbance spectra of soil.

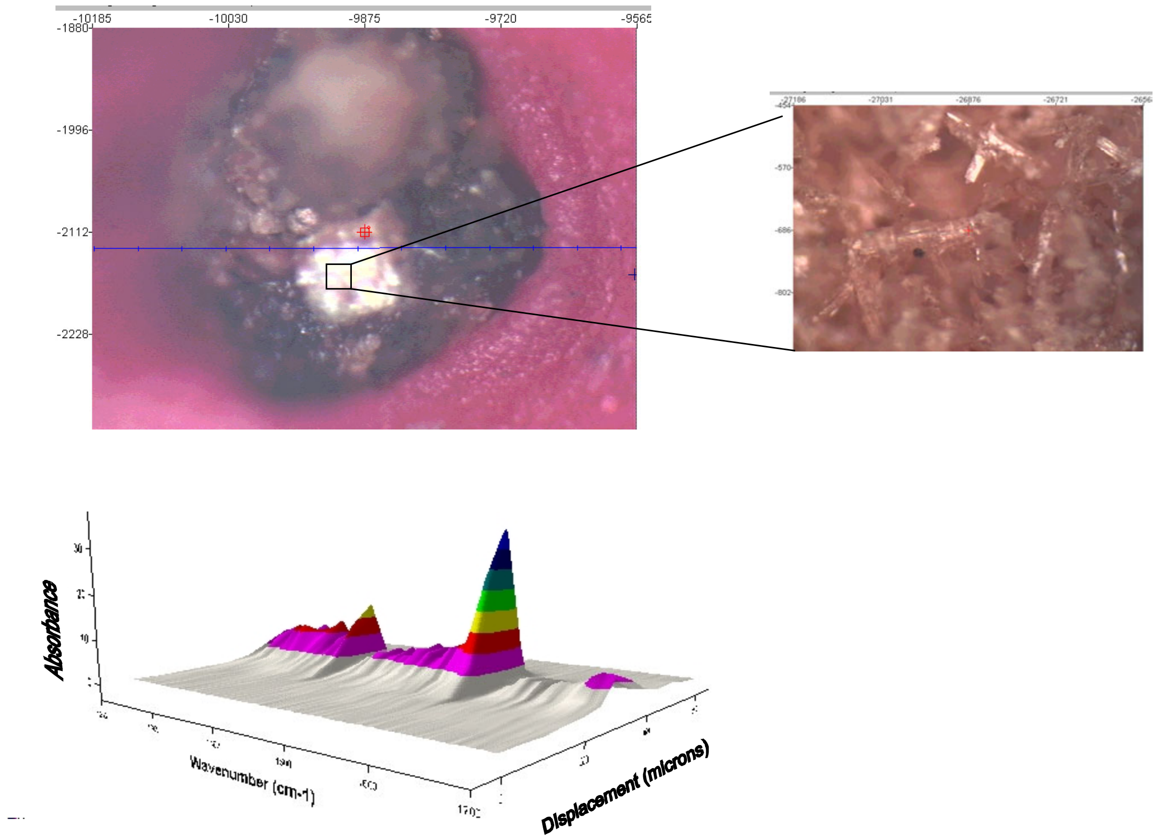

Figure 2. Top picture shows a soil particle with a white crystalline spot that was identified as crystalline TNT based on IR spectral map shown below. Contour map below shows IR absorbance along the blue line across the soil particle. The two prominent NO_2 stretch vibrations indicate a strong presence of TNT in the white spot. Image on the right shows a magnified image of the crystalline nature of TNT seen embed in the soil particle.

REFERENCES:

1. Daun, G.; H. Lenke; M. Reuss; H-J. Knackmuss. Environ. Sci. Technol. **33**, 2617, 1998.
2. Pennington, J.C.; C.A. Hayes; K.F. Myers; M. Ochman; D. Gunnison; D.R. Felt; E.F. McCormick. Chemosphere **30**, 429, 1995.
3. Sheremata, T.W.; S. Thiboutot; G. Ampleman; L. Paquet; A. Halasz; J. Hawari. Environ. Sci. Technol. **32**, 4002, 1998.
4. U. Ghosh, R.G. Luthy, J.S. Gillette and R.N. Zare. Environ. Sci. Technol, **34**, 1729, 2000.
5. J.W. Talley U. Ghosh, S.G. Tucker, J.S. Furey, and R. G. Luthy. Environ. Sci. Technol, (in press).

Funding for this work was provided by the US Army Waterways Experiment Station, Vicksburg, MS.

Contact Information: Dr. Upal Ghosh, Department of Civil and Environmental Engineering, Stanford University, Stanford CA 94305. Email: ughosh@stanford.edu. Telephone: 650-723-5885. URL: http://www.stanford.edu/~ughosh

Monitoring anthropogenic metal released in the environment via X-ray fluorescence, absorption and diffraction at micrometer scales of resolution

A. Manceau[1,2], M.A. Marcus[1], N. Tamura[1], R.S. Celestre[1], A.A. MacDowell[1], R.E. Sublett[1], H.A. Padmore[1], M. Kersten[3]

[1]Advanced Light Source, Lawrence Berkeley National Laboratory, Berkeley, CA 94720

[2]Environmental Geochemistry Group, Hilgard Hall, University of California, Berkeley, CA 94720

[3]Geoscience Institute, Gutenberg University, 55099 Mainz, Germany

INTRODUCTION

Ferromanganese nodules are common in aquatic systems, including lacustrine and shallow marine environments, and also on the oceanic seafloor. They generally have a banded structure consisting of practically pure and alternating Fe- and Mn-rich layers separated by mixed Fe-Mn zones. This concretic onion-like growth pattern is attributed to intermittent oxidizing and reducing conditions. Accretion of ferromanganese nodules may cover time scales up to millions of years. The implication that they provide a continuously growing substrate with constant sorption efficiency for trace elements is the basis of a resuming interest for Fe-Mn nodules focusing on their possible use as a paleoproxy record for long-term environmental changes. Therefore, an idea was born to try and assess the metal fluxes into the ferromanganese nodules by dating individual nodule growth layers, and to compare these fluxes with the temporal variability in anthropogenic emissions. The prerequisite for such an approach is high-resolution profiling due to the slow accretion of the nodule material. Synchrotron-based micro-X-ray fluorescence (µSXRF) was applied to obtain in-situ trace element profiles of the necessary spatial resolution, as a basis for the evaluation of nodule accretion rates and for an assessment of their use for retrospective monitoring of excess metal input in the western Baltic Sea. Then, in-situ X-ray diffraction (XRD) and extended X-ray absorption fine structure (EXAFS) spectroscopy at the Mn and Zn K-edge were performed at the micrometer resolution to determine how anthropogenic Zn is taken up.

EXPERIMENTS

The examined nodule was collected in shallow water of the SW Baltic Sea where nodules are relatively fast-growing and enriched in metal contaminants, thus making them highly suitable to record the anthropogenic pollution in the last century. The sample was prepared as a micropolished 30 µm-thick thin section. The µXRD patterns of Fe- and Mn-pure layers were recorded on Beamline 7.3.3., and µEXAFS spectra were collected on Beamline 10.3.2. In both experiments, µSXRF maps were first recorded to image the Fe and Mn layers. All experiments were conducted with a beamsize of 15 (H) x 5 to 10 (V) µm.

RESULTS AND INTERPRETATION

The µSXRF element map of Fe and Mn (Fig. 1) shows the typically cuspate zebra-type band structure of the Fe-Mn concretions. The thickness of Mn-rich layers varies typically from 200 to 500 µm and that of the Fe-rich layers from about 100 to 200 µm. Of the trace elements investigated (Co, Ni, Cu, and Zn), Zn showed the most significant enrichment, with values in the outermost surface Mn layers of up to six-fold higher than those found in older core parts. Thus, the high-resolution Zn profiles provide the necessary temporal resolution for a dating method analogous to dendrochronology. Assuming a continuous accretion of these relatively fast growing nodules (on average 20 μm yr^{-1}) over the last century, the Zn enrichment was assessed to have commenced in 1880/90, reflecting the enhanced heavy metal emissions with rising industrialization in Europe. μXRD patterns collected in Fe-rich regions (Fig. 2) contain only a broad and faint double hump with maxima at about 2.85 Å and 2.25 Å. The centroid of this hump is at about 2.5 Å as in poorly-crystallized two-line ferrihydrite (hydrous ferric oxide). Minor amounts of detrital quartz grains and silica particles (opal-A) were also detected by μXRD. The μXRD patterns taken in the Mn-rich layers look completely different consisting of a series of basal reflection peaks at 7.07 Å (001), 3.51 Å (002) and *hk*0 peaks at 2.46 Å (200) and 1.43 Å (110). These peak positions, together with the noteworthy asymmetrical shape of the (200) reflection, are characteristic of turbostratic hexagonal birnessite (δ-MnO_2).

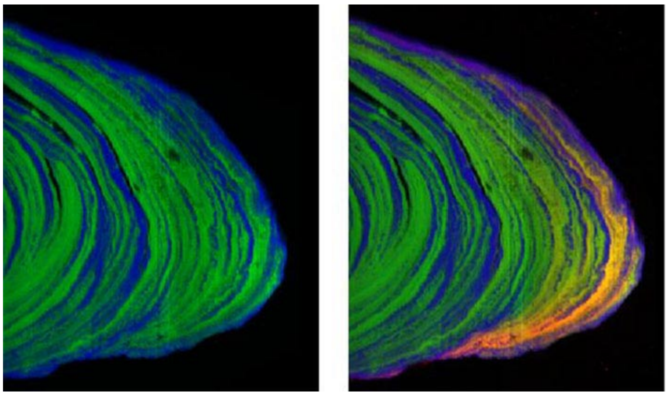

Figure 1. Synchrotron-based micro-X-ray radiation fluorescence (μSXRF) Fe and Mn maps of the outermost Fe and Mn layers of a ferromanganese nodule from the Baltic sea (6600 μm x 3780 μm, step size 15 μm, counting time 250 ms/pixel, red = Zn, green = Mn, blue = Fe, beamline: 10.3.2.). The onion-like structure of growth rims is clearly discernible as few hundreds μm thick Fe/Mn-rich bandings. Zn is exclusively associated with Mn, as indicated by the orange color of the Zn-containing Mn layers, and its concentration increases towards the surface.

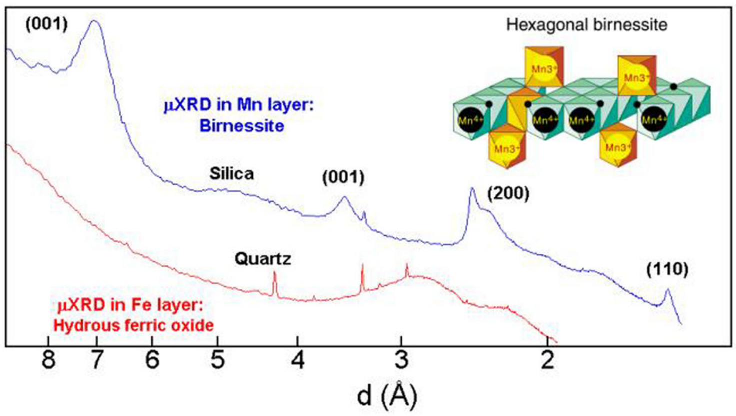

Figure 2. X-ray microdiffractograms collected in Mn (λ = 1.252 Å) and Fe (λ = 1.758 Å) layers. Mn is speciated as turbostratic hexagonal birnessite (δ-MnO_2), and Fe as hydrous ferric oxide. Quartz grains (sharp peaks) and silica particles (d ≈ 4.6 Å) were detected throughout the sample.

To determine the Zn sorption mechanism at the molecular-level, Zn K-edge μEXAFS spectra were collected in a Zn 'hot spot'. Qualitative information about the local structure of Zn can be obtained by comparing the unknown μEXAFS spectrum to reference EXAFS spectra from relevant model compounds. The best spectral match was obtained with the Zn-sorbed birnessite reference, in which Zn is predominantly tetrahedrally, and secondarily octahedrally, coordinated and complexed above vacant sites of the manganese layer (Fig. 3). Comparison of radial structure functions (Fig. 3b) indicates that the Zn-O and Zn-Mn distances are both slightly, but significantly, shortened in the nodule sample, which is indicative of the presence of only ^{IV}Zn. The preferred formation of the ^{IV}Zn over the ^{VI}Zn complex presumably arises from the presence of aliovalent Mn^{3+} ions within the MnO_2 layer, because 4-fold coordinated Zn provides more positive charges to undersaturated oxygens (2+/4 = 0.5 v.u.) than a 6-fold coordinated Zn (2+/6 = 0.33 v.u.).

CONCLUSION

This study demonstrates the merit of deploying in parallel fluorescence, diffraction, and absorption studies at micrometer scales of resolution. This unprecedented combination of techniques allows the determination of the structural form of trace elements in heterogeneous matrices with an unequaled precision. Since much of nature and synthetic materials are heterogeneous on micron and sub-micron length scales, we anticipate that the synergistic use of µSXRF, µSXRD, and µEXAFS will have broad applications and add to the arsenal of analytical methods available in environmental and materials science.

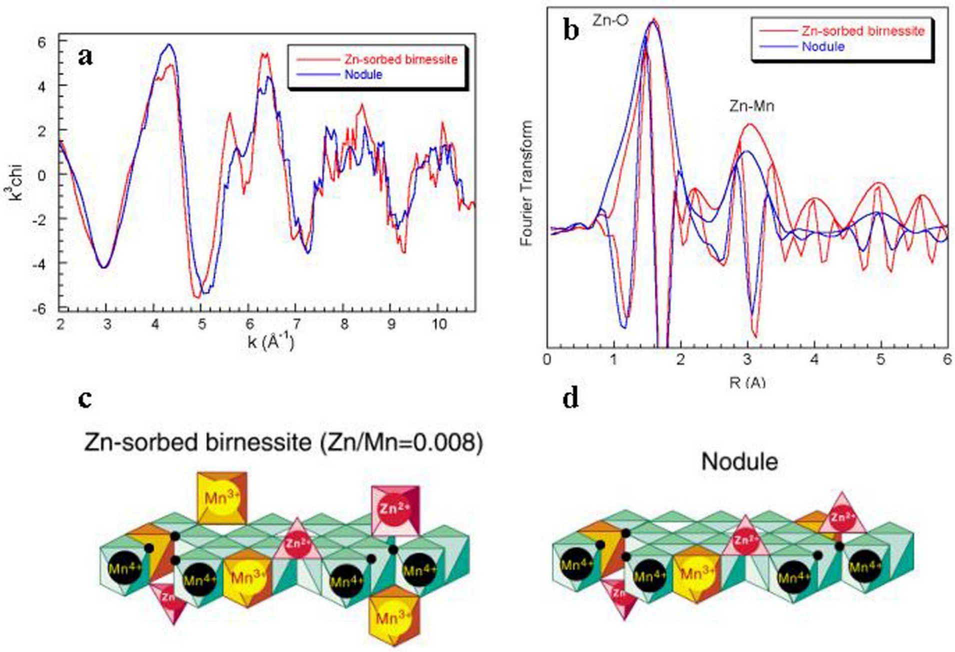

Figure 3. Zn K-dge µEXAFS spectrum and Fourier transform (modulus plus imaginary part) from a Zn 'hot spot' of the nodule rim presented in Fig. 1, compared to the Zn-edge data from a Zn-sorbed birnessite reference, in which Zn is sorbed as a mix of ^{IV}Zn and ^{VI}Zn complexes above vacant layer Mn sites. The unknown and reference data look similar, indicating that Zn are uptaken in a similar manner in the two compounds. However, Zn-O and Zn-Mn distances are clearly shorter in the natural sample because Zn is only four-fold coordinated.

This work was supported by the Director, Office of Energy Research, Office of Basic Energy Sciences, Materials Science Division, of the U.S. Department of Energy under Contract No. DE-AC03-76SF00098.

Principal investigator: Alain Manceau, Advanced Light Source, Ernest Orlando Lawrence Berkeley National Laboratory. Email: acmanceau@lbl.gov. Telephone: 510-643-2324.

New IR microscope and bench installed at BL1.4

Michael C. Martin[a], Hoi-Ying N. Holman[b], and Wayne R. McKinney[a]
[a] Advanced Light Source Division, Lawrence Berkeley National Laboratory, Berkeley, CA 94720
[b] Center for Environmental Biotechnology, Lawrence Berkeley National Laboratory, Berkeley, CA 94720

1. INTRODUCTION

New infrared spectromicroscopy equipment was purchased for and installed on the ALS infrared beamlines on beam port 1.4. It includes the latest step-scan capable FTIR bench and an infinity corrected infrared microscope which will allow for a number of new sample visualization methods. This equipment was purchased with funding from the DOE Office of Biological and Environmental Research (OBER) with the express purpose to develop biomedical and biological applications of synchrotron-based infrared spectromicroscopy.

2. EQUIPMENT

The new spectromicroscopy equipment includes a Thermo Nicolet Nexus 870 step- and rapid-scan FTIR bench, and a Thermo Spectra-Tech Continuum IR microscope, photographed below. The IR microscope includes two IR detectors, a wide-band MCT and a fast (20 ns) TRS MCT for time-resolved experiments. A fast digitizer (up to 100MHz) compliments the TRS MCT detector. The synchrotron beam coupled into the IR microscope continues to have a diffraction-limited spot size, thereby attaining a 200-fold increase in signal from small (3 – 10 micron) sample spot compared to a conventional thermal IR source. The infinity-corrected microscope optics allow for a number of additional sample visualization accessories which can help the user identify the important location within their sample for micro-IR analysis:

- Visual and IR polarizers
- Dark-field illumination
- DIC (Differential Interference Contrast) optics
- UV Fluorescence

An example of DIC optics enhancing a micrograph of human cheek cells is shown in the photograph to the right. The DIC technique provides a psuedo-3D effect, enhancing the contrast between different thicknesses of an otherwise clear sample. In the image to the right, one can make out the nuclei of the cells (thicker bump near the middle of each cell), whereas this would be difficult using conventional illumination.

This new instrument will aide in user scientific research across many fields. For example, the study of individual living cells, toxic contaminants, bioremediation, protein microcrystals, rhizoids, and forensic evidence will all be enhanced by the additional capabilities of this new SR-FTIR spectromicroscopy system.

ACKNOWLEDGEMENTS

This research was supported by the Office of Science, Office of Biological and Environmental Research, Medical Science Division and the Office of Science, Office of Basic Energy Sciences, Materials Sciences Division, of the U.S. Department of Energy under Contract No. DE-AC03-76SF00098 at Lawrence Berkeley National Laboratory.

Principal investigator: Michael C. Martin, Advanced Light Source Division, LBNL, 510-495-2231, MCMartin@lbl.gov

O 1s XAS of H_2O in the solvation shell of monovalent and trivalent ions

L.Å. Näslund[1], Ph. Wernet[2], H. Ogasawara[1], D. Edwards[3], S. Myneni[3] and A. Nilsson[1,2]

[1]Stockholm University, SCFAB, Fysikum, S-106 91 Stockholm, Sweden
[2]SSRL, 2575 Sand Hill Road, MS 69, Menlo Park, CA94025, USA
[3]Department of Geosciences, Princeton University, Princeton, NJ 08544, USA

INTRODUCTION

Earlier experiments with the Soft X-ray Endstation for Environmental Research (SXEER) have shown that pure liquid water consists of three different species of water molecules - symmetric (SYM), acceptor asymmetric (A-ASYM), and donator asymmetric (D-ASYM) [1]. By dissolving Potassium Chloride or Aluminum Chloride we introduce a fourth type of water species - water molecules in the solvation shell of the dissolved ions. X-ray Absorption Spectroscopy at the oxygen K-edge (O 1s XAS) gives the information of Oxygen p-character and hence the local geometric arrangement around the probed oxygen atom. In this report we will show some of the XAS spectra we have obtained at beamline 8.0.

O 1s XAS OF WATER WITH DISSOLVED KCl AND $AlCl_3$

If we dissolve Potassium Chloride (KCl) into water, the water molecules will form a solvation shell around each Potassium- and Chloride ion. These water molecules will have a different electronic structure than a water molecule in the bulk water. We can actual say that we have a fourth water species. Figure 1 is showing a XAS spectrum at the oxygen edge of water with dissolved KCl. We can see changes in two energy ranges. The pre-edge at 535 eV has higher intensity and has a shoulder at 534.3 eV. This is probably due to changes in the distribution of D-ASYM water species in the bulk water. The higher intensity at 537.0 eV can be explained by water molecules in the solvation shell of K^+ ion. Preliminary calculations are supporting the experimental data.

Comparing water dissolved KCl with water dissolved Aluminum Chloride ($AlCl_3$) can give some input to the interpretation. An O 1s XAS spectrum of water with dissolved $AlCl_3$ is shown in figure 2. As in dissolved KCl there is a shoulder at 534.3 eV. For water with dissolved $AlCl_3$ the shoulder is more distinct and indicates that the feature at 535 eV is a double peak. However, the interpretation is the same as in the case of dissolved KCl - there are changes in the distribution of D-ASYM water species in the bulk. At higher energy the O 1s XAS spectrum of water with dissolved $AlCl_3$ is showing higher intensity than pure water. If we compare the spectrum of water dissolved $AlCl_3$ with water dissolved KCl we can see that water dissolved $AlCl_3$ have lower intensity at 537.0 eV and higher intensity at 540.5 eV. This can be explained by differences in the electronic structure of water molecules in the solvation shell of trivalent ions from that of monovalent ions. Preliminary calculations show that the fourth water species, water molecules in the solvation shell of the Al^{3+} ion, is giving higher intensity in a different energy range than the water molecules in the solvation shell of the K^+ ion.

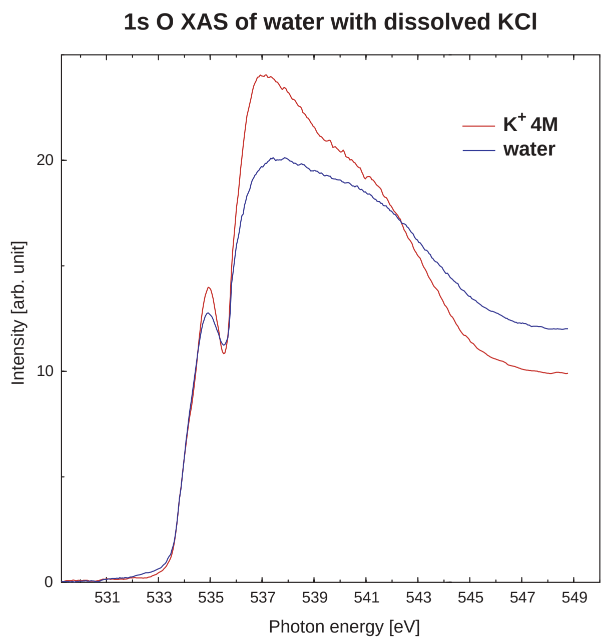

Figure 1. Oxygen 1s XAS of water with dissolved Potassium Chloride (KCl) compared to pure water. The spectrum of water with dissolved KCl has a shoulder at 534.3 eV. It is easier seen in figure 2.

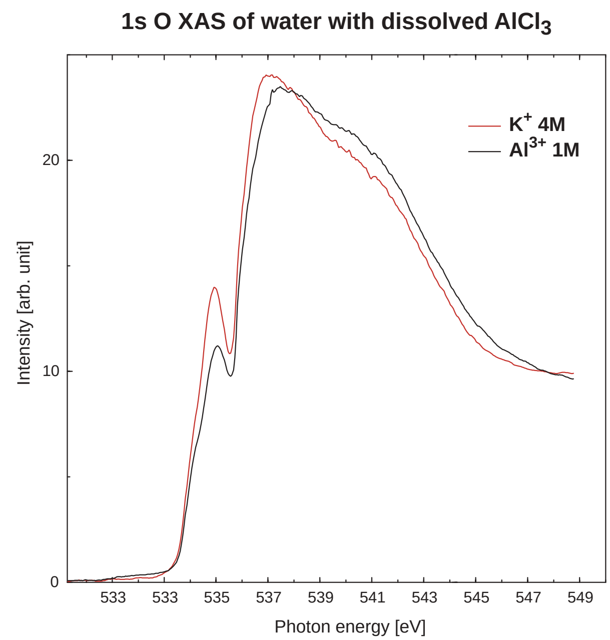

Figure 2. Oxygen 1s XAS of water with dissolved Aluminum Chloride ($AlCl_3$) compared to water with dissolved Potassium Chloride (KCl).

CONCLUSION

We have shown that O 1s XAS is sensitive enough to resolve the electronic structure of water molecules in a solvation shell of an ion. As an example we have presented differences in the O 1s XAS spectrum between pure liquid water, water with dissolved KCl and water with dissolved $AlCl_3$. The distribution of the D-ASYM water species in bulk water is changing when KCl or $AlCl_3$ is dissolved in the water. Further investigation will tell how the distribution is changed.

ACKNOWLEDGMENTS

M. Cavalleri and L.G.M Pettersson at Fysikum, University of Stockholm have done the preliminary calculations and are involved in the analyzing of the data collected at Beamline 8.0.

REFERENCES

1. S. Myneni, Y. Luo, L.Å. Näslund, M. Cavalleri, L. Ojamäe, H. Ogasawara, A. Pelmenschikov, Ph. Wernet, P. Väterlein, C. Heske, Z. Hussain, L.G.M. Pettersson, and A. Nilsson, *Journal of Physics: Condensed Matter, In press*

This work is supported by the Basic Energy Sciences (Geosciences, Department of Energy, USA), the Swedish Royal Academy of Science (KVA), and the Göran Gustafssons Foundation for Research in Natural Science and Medicine.

Principal investigator: S. Myneni, Department of Geosciences, Princeton University, Princeton, NJ 08544, USA. Email: smyneni@Princeton.EDU. Telephone: 609-258 5848.

Spatial Distribution of Bacteria on Basalt Using SR-FTIR

Mary E. Kauffman,[†,1,2] Hoi-Ying Holman,[3] R. Michael Lehman,[2] Michael C. Martin[4]

[1]Idaho State University, Depts. Of Biologiy and Geology, Pocatello, ID, 83209, [2]Idaho National Engineering and Environmental Laboratory (INEEL), Idaho Falls, ID, 83415, [3]Center for Environmental Biotechnology, Lawrence Berkeley National Laboratory, Berkeley, CA, 94720, [4]Advanced Light Source, Lawrence Berkeley National Laboratory, Berkeley, CA, 94720. [†]Address correspondence to Mary E. Kauffman, INEEL, Geomicrobiology Group, PO Box 1625, MS 2203, Idaho Falls, ID, 83415. Email:kaufme@inel.gov

INTRODUCTION

Understanding the role of microorganisms on the fate and transport of contaminants is essential in the determination of risk assessment and the development of effective remediation strategies for contaminated sites. The microscale distribution of microorganisms on the surface of complex geologic media will affect the types and rates of biotransformations in contaminated environmental systems. In this study, we used synchrotron radiation-based Fourier transform infrared spectromicroscopy (SR-FTIR) at the Advanced Light Source (ALS) Beamline 1.4.3, Lawrence Berkeley National Laboratory (LBNL), to investigate the preferential attachment of *Burkholderia cepacia* G4 to the various mineral phases within basalt. SR-FTIR is a non-destructive, in situ analytical tool, that when coupled to an automated X, Y positioning stage, can provide surface mapping of biochemical functional groups.

MINERAL AND BASALT SPECIMENS

Basalt specimens were prepared from core samples. The center of the core was cut into 1” square blocks and then sliced into specimens 1 mm thick using a diamond saw blade and water as the lubricant. Mineral standards for the four major mineral phases in basalt (plagioclase, augite, ilmenite and olivine) were prepared in the same fashion. The specimens were sonicated and autoclaved prior to use. Basalt and mineral specimens were spectrally characterized using SR-FTIR prior to, and after, exposure to a bacterial growth culture for several days. SR-FTIR spectra of the distinct mineral phases in the basalt were compared to spectra obtained for individual mineral standards.

BACTERIAL CELLS, CULTURES AND CONDITIONS

Burkholderia cepacia G4 was selected as the model organism for this study due to the fact that it is a common soil microorganism, and therefore representative of bacteria found in environmental systems. Microcosms consisting of basalt or mineral specimens and bacterial culture solution were placed on a rotary shaker (55 rpm) at 23 ° C for five days. The culture solutions were changed daily and new inoculum was added. At the end of the five days, the specimens were removed from solution and rinsed with phosphate buffer to remove any loose cells.

SR-FTIR SPECTROMICROSCOPY

SR-FTIR spectra were collected at Beamline 1.4.3 at the ALS, LBNL, Berkeley, CA. All SR-FTIR spectra were recorded in the 4000-650 cm^{-1} infrared region. This region contains absorbance features correlative to characteristic IR-active vibrational modes for common biomolecules such as nucleic acids, proteins and lipids, as well as identifying absorbance features for the basalt and mineral specimens. Spectral maps of the basalt surfaces were obtained by programming the microscope X-Y positioning stage to collect spectra at specific step locations and then extracting spatial information of functional groups based upon absorbance peak wavenumbers. Data was collected in single-beam reflectance mode with a spectral resolution of 4 $cm^{-1}$and 64 scans were co-added for Fourier transform processing for each spectrum. Each resulting spectrum was then ratioed to the spectrum of a gold slide to produce absorbance values. By extracting each individual spectrum within the mapping grid and comparing it to spectra collected on each of the four individual minerals, identification of the underlying mineralogy can be determined. Figure 1 shows the spatial distribution of bacteria on a basalt surface, based upon the occurrence of the protein amide I peak at ~1650 cm^{-1}, and the preferential attachment by *B. cepacia* G4 to plagioclase. The total map area was 250 X 105 μm with spectra collected every 25 μm along the X coordinate and every 15 μm along the Y coordinate. Correlative maps of the same surface area were constructed based upon the protein amide II peak at ~1550 cm^{-1} and at least one other absorbance feature related to the presence of biomolecules, to insure the resulting map was due to the spatial distribution of bacteria and not an artifact of the mineralogy (data not shown).

RESULTS

Multiple SR-FTIR maps of basalt surfaces colonized by bacterial cultures showed preferential attachment by *B. cepacia* G4 to plagioclase within the basalt matrix. The mineral apatite ($Ca_5(PO_4)_3(F, Cl, OH)$) is a common accessory mineral in igneous rocks and appears as inclusions in igneous plagioclase feldspars. Phosphorous is required by bacterial cells for the synthesis of nucleic acids and phospholipids. Scanning electron microprobe results indicate the presence of phosphorous in both the plagioclase within the basalt matrix and in the Ward's standard plagioclase specimen (data not shown). A recent study on feldspars as a source of nutrients determined that microorganisms extracted inorganic phosphorous from apatite inclusions in alkaline feldspars. It is highly likely that *B. cepacia* G4 preferentially attaches to the calcic plagioclase in order to access phosphorous from apatite inclusions.

This work was supported by the Idaho National Engineering and Environmental Laboratory.

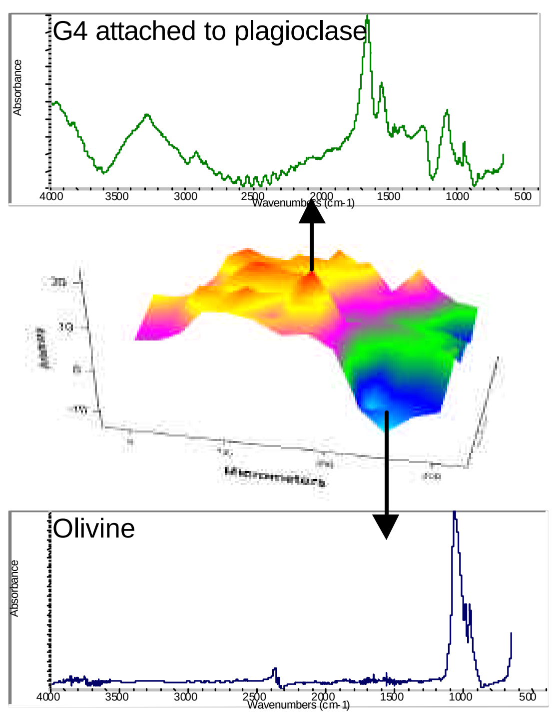

Figure 1.

SR-FTIR Study of Bacteria-Water Interactions: Acid-base Titration and Silification Experiments

Nathan Yee[1], Liane G. Benning[1], Mark J. Tobin[2], and Kurt O. Konhauser[1]

[1]School of Earth Sciences, University of Leeds, United Kingdom
[2]Synchrotron Radiation Source, Daresbury Laboratory, United Kingdom

Bacterial surfaces are highly reactive and can strongly affect mass transport in a wide range of geological environments. Bacterial cell walls can adsorb aqueous metal cations, and can act as nucleation surfaces for heterogeneous mineral precipitation. However, the reactions at the bacteria-water interface are poorly understood, primarily due to the difficulty in monitoring such processes *in situ* and *in vivo*. In this study, we use synchrotron radiation-based FTIR to investigate the chemistry of bacterial surfaces with acid/base titration and Si precipitation experiments. The objectives of this research are to identify the reactive surface functional groups and to determine how metal adsorption/precipitation affects the protein and lipid structures of individual living bacterial cells. *In-situ* FTIR experiments were performed on the Infrared beamline 1.4.3 at the Advance Light Source (Lawrence Berkeley National Laboratory), using a Nicolet 760 FTIR bench and a Spectra-Tech Nic-Plan IR microscope. All experiments were performed with flow through fluid cell with BaF_2 and ZnSe windows separated by a 6 um mylar spacer. Acid-base titration and Si precipitation experiments were conducted with both intact cells and isolated bacterial sheaths of *Calothrix* (strain KC97) a filamentous cyanobacteria. Titration experiments with intact bacterial cells show a change in peak position of the carboxylic functional group at ~1400 cm^{-1} (symmetric vibrational stretching of deprotonated carboxylate groups) from acidic to near-neutral pH (Fig 1). The bacterial silicification experiments indicate a change in peak position at ~ 1700 - 1740 cm^{-1}, corresponding to the vibrational C=O stretching of esters groups in the lipid structures of the cell (Fig 2). Previous studies have demonstrated that hydrogen bonding onto carbonyl functional

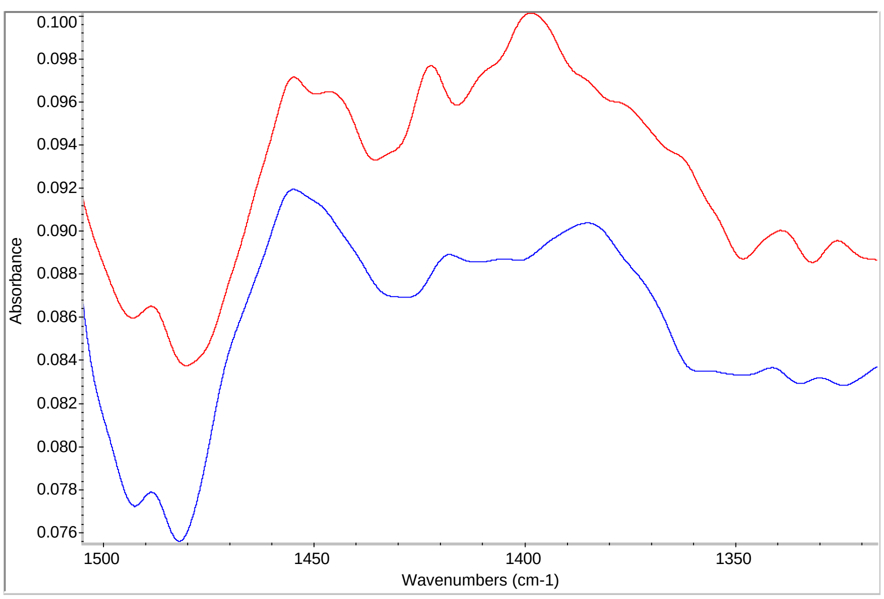

Figure 1. Infrared spectra of an intact *Calothrix* cell in aqueous solution at pH 2.9 and 6.3. A shift in peak position is observed at 1400 cm^{-1} corresponding to $v_s(COO^-)$ stretching of deprotonated carboxylate functional groups.

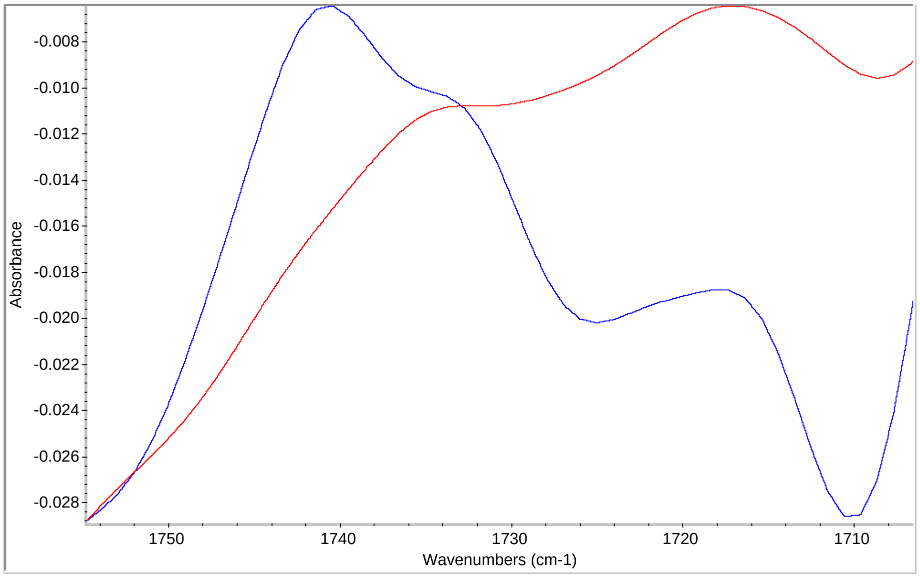

Figure 2. Infrared spectra of an intact *Calothrix* cell before and after silicification. A change in peak position of vibrational C=O stretching is observed.

groups can shift the peak positions in this wavenumber range. Finally, infrared microspectrometry experiments were performed to image the proteins, lipids, and nucleic acids inside intact living cells. Spatial resolution of a few microns was achieved and the chemical distribution of proteins was mapped throughout a *Calothrix* filament (Fig 3). The data indicate that protein molecules have a high concentration within the cell, but a very low concentration on the bacterial surface. These results demonstrate that SR-FTIR can be applied to investigate the functional group chemistry of bacteria in a range of different bacteria-water systems.

This work is an ENVIROSYNC project funded by the Natural Environmental Research Council, UK.

Principal investigator: Liane Benning, University of Leeds, +44-113-233-5220, liane@earth.leeds.ac.uk.

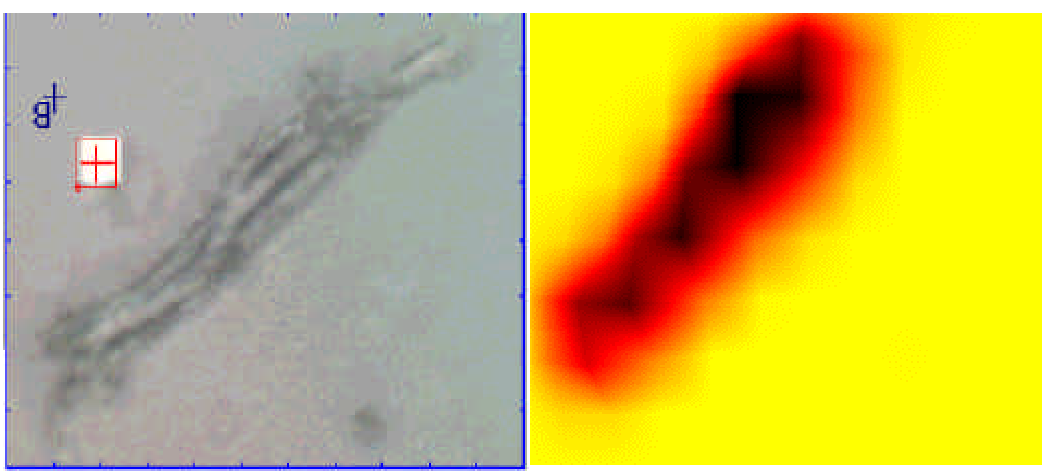

Figure 3. Chemical distribution of the protein characteristic bands amide I and amide II (1495-1800cm^{-1}) of a *Calothrix* filament. a) Optical image, b) 2-D map of the protein distribution.

Surface spectroscopy of nano-scale reactions in aqueous solution

K. H. Pecher[1,2] and B. Tonner[2]
[1]currently at: Advanced Light Source, Ernest Orlando Lawrence Berkeley National Laboratory, University of California, Berkeley, California 94720, USA
[2]Depaartment of Physics, University of Central Florida, Orlando, Florida 32816-2385, USA

INTRODUCTION

The rate of oxidation of dissolved Mn(II) by oxygen is enhanced in the presence of catalytic surfaces. Surfaces of iron oxides such as Goethite (α-FeOOH), Lepidocrocite (γ-FeOOH), and Hematite (α-Fe_2O_3) can increase the rate of Mn(II) oxidation over the initial homogeneous solution rate by orders of magnitude [1, 2]. These reactions are further complicated by the observation that initially formed reaction products are metastable and depend strongly on both the bulk reaction conditions such as temperature, concentration of Mn(II), pH-value, presence of dominant anions [3-5], and interfacial reaction conditions existing at the catalytic surfaces. The activities of reactants and products and especially the thermodynamic properties of Mn(III) species at such surfaces are not known and are not readily measurable [4]. In addition, initially formed Mn-oxides or hydroxides may autocatalytically enhance reaction rates [6]. A contribution from autocatalytic oxidation of Mn(II) has been hypothesized for the formation of Mn-micronodules in lake sediments [7] and the occurrence of Mn-biominerals formed by spores of a marine bacillus *SG-1* [e.g. 8, 9]. It is therefore quite natural that details on the identity of reaction products vary a lot in the literature.

Traditionally, two different approaches have been utilized to study Mn(II) oxidation at mineral surfaces: a macroscopic approach using wet chemistry data and surface complexation models [10], and a microscopic approach using Scanning Force Microscopy and surface spectroscopic techniques [11]. Junta-Rosso et al. [12] have also tried to link both microscopic and macroscopic data to develop rate expressions that are consistent with both approaches. The microscopic as well as surface spectroscopic techniques applied in those studies suffer from transfer of wet samples into high vacuum, the effect of which has not yet been studied systematically. We have used Scanning Transmission X-ray Spectromicroscopy (STXM) to characterize products formed during the heterogeneous oxidation of Mn(II) by dissolved oxygen on fully hydrated single nano-sized particles of catalytically active iron oxides.

MATERIALS AND METHODS

Aliquots of powdered iron oxides (Goethite, Lepidocrocite, and Hematite) equivalent to 25 m^2L^{-1} were each suspended in 10 mM HEPES solution (pH 7.8, 50 mM NaCl) and equilibrated for 24 h. Characteristics of the used iron oxides are given elsewhere [13]. These suspensions were kept open to atmosphere on a multi stirring plate and were repeatedly spiked with aliquots from a 55 mM $MnCl_2$ stock solution. Time intervals between sequential addition of Mn(II) were chosen long enough to keep the concentration of dissolved Mn(II) below 0.3 mM.
Two sets of samples were withdrawn for STXM measurements: (a) after 96 d of reaction time and a total Mn(II)-dosage of 244 μM, and (b) after 129 d of reaction time and a total Mn(II)-dosage of 1.26 mM. All X-ray absorption measurements were done at the Advanced Light Source (Lawrence Berkeley National Laboratory) on beam line 7.0.1. Sample preparation and

technical specifications of an upgrade version of STXM are given elsewhere [14, 15]. Data analysis and spectral interpretation using XANES of reference compounds are detailed in [16].

RESULTS AND DISCUSSION

STXM of the first set of samples withdrawn after 96 days and a total Mn(II) dose of 244 µM, did not result in detectable amounts of Mn on the iron oxide particles. Obviously, the mass of adsorbed Mn(II) and/or oxidation products present on the particles were below the detection limit of the instrument. Figure 1 shows single needles of Goethite after 129 d of incubation imaged at the Fe absorption maximum and the corresponding XANES of the Mn-edge. The spectrum could be fitted by a linear combination of spectra of single valent Mn(II) and Mn(III)-reference models. Fits did not improve by including any Mn(IV)-component.

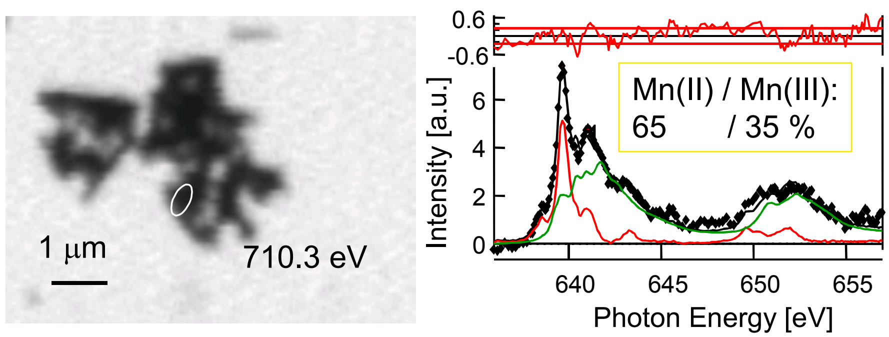

Figure 1. Image of single needles of Goethite (left) and XANES (◆) at the Mn-edge extracted from the area labeled on the image. The XANES is fitted to a linear combination of spectra of single valent reference compounds (red: $MnSO_4$, green: γ-MnOOH). Quantitative results are given in mass % of each charge component and residuals are plotted with the horizontal lines indicating ± one standard deviation.

Under the experimental conditions used, the iron oxide catalyzed oxidation of Mn(II) led to a mixed valent Mn(II)/Mn(III)-species (most likely Hausmannite [4,5]), the stoichiometric ratio of which might be superimposed by specific adsorption of Mn^{2+} from solution. Control experiments under anoxic conditions are necessary to decide whether the high Mn(II)-content is due to adsorption of Mn^{2+} onto iron oxide surfaces or incorporation into oxidation products. Within the time frame of our experiment, we can rule out disproportionation of initial Mn(III)-species, although this reaction is thermodynamically favorable under our bulk reaction conditions. We hypothesize that reaction conditions at the iron oxide interfaces can stabilize Mn(III). Comparing the mass fraction of Mn(III) on all three iron oxides, the order is α-FeOOH»α-Fe_2O_3>γ-FeOOH, which does not correlate with the amount of specific sites for cation sorption on those oxides. The observed order, however, does correlate with the order of catalytic activities observed during reductive dehalogenation of polyhalogenated methanes by Fe(II) sorbed to exactly the same iron oxides [13]. We conclude that unknown steric/electronic properties of the iron oxide substrates might be involved as controlling factors in lowering the redox potential of transition metal cations sorbed to such surfaces.

ACKNOWLEDGMENTS

Thanks to Sirine Fakra, Rick Steele and Tony Warwick for providing such a wonderful instrument. Adam Hitchcock and Eli Rotenberg provided software for data analysis.

REFERENCES

[1] Diem, D.; Stumm, W. Geoch. et Cosmoch. Acta 1984, 48,1571-1573.
[2] Sung, W.; Morgan, J.J. Geoch. et Cosmoch. Acta 1981, 45,2377-2383.
[3] Hem, J.D. Geoch. et Cosmoch. Acta 1981, 45,1369-1374.
[4] Hem, J.D.; Lind, C.J. Geoch. et Cosmoch. Acta 1983, 47, 2037-2046.
[5] Murray, J.W.; Dillard, J.G.; Giovanoli, R.; Moers, H.; Stumm, W. Geoch. et Cosmoch. Acta 1985, 49,463-470.
[6] Murray, J.W. Geoch. et Cosmoch. Acta 1975, 39,505-519.
[7] Murray, L.W.; Balistrieri, L.S.; Paul, B. Geoch. et Cosmoch. Acta 1984, 48,1237-1247.
[8] Nealson, K.H.; Tebo, B.M. Adv. Appl. Microbiol. 1988, 33,279-318.
[9] Mandernack, K.W.; Post, J.; Tebo, B.M. Geoch. et Cosmoch. Acta 1995, 59,4393-4408.
[10] Davies, S.H.R.; Morgan, J.J. J. Colloid Interface Sci. 1989, 129,63-77.
[11] Junta, J.L.; Hochella Jr., M.F. Geochim. Cosmochim. Acta 1994, 58,4985-4999.
[12] Junta-Rosso, J.L.; Hochella Jr., M.F.; Rimstidt, J.D. Geoch. et Cosmoch. Acta 1997, 61,149-159.
[13] Pecher, K.; Haderlein, S. B.; Schwarzenbach, R. P. Environ. Sci. Technol. 2001 accepted.
[14] http://www-esg.lbl.gov/Stxm/
[15] Pecher, K.; Kneedler, E.; Rothe, J.; Meigs, G.; Warwick, T.; Nealson, K.; Tonner, B. In: X-ray Microscopy (XRM´99); AIP Conference Proceedings 507, W. Meyer-Ilse, T. Warwick, D. Attwood (Eds.); Berkeley, 2000; p 291-300.
[16] Pecher, K.; McCubbery, D., Kneedler, E.; Rothe, J.; Bargar, J.; Meigs, G.; Cox, L., Nealson, K.; Tonner, B. submitted to Geoch. et Cosmoch. Acta 2001.

This work was supported by the Director, Office of Energy Research, Office of Basic Energy Sciences, Materials Science Division, of the U.S. Department of Energy under Contract No. DE-AC03-76SF00098. This work was supported by grants from DOE Division of Materials Sciences FG02-98ER45688 and DOE NABIR FG02-97ER62474.

Principal investigator: Klaus Pecher, Advanced Light Source, Ernest Orlando Lawrence Berkeley National Laboratory. Email: khpecher@lbl.gov. Telephone: 510-495-2232.

The use of micro-FTIR to characterize soil minerals and Boron adsorption

S. Pittiglio and H.E. Doner
Ecosystem Sciences Division – Environmental Science, Policy and Management,
University of California, Berkeley, California 94720-3110, USA

INTRODUCTION

This study was carried out in an effort to obtain direct structural information of adsorbed boron on the solid surfaces of soil material (clays and oxides). It is necessary to understand the relationship between trace elements and clays at a molecular level to describe and predict interfacial processes controlling trace element retention and release in soils. Our goals for this last proposal period were: 1) to build a spectral library of clay minerals, oxides and boron containing minerals commonly found in California soils. This library would be used to conjunction with x-ray diffraction (XRD) data to determine if micro-Fourier transformed infrared spectroscopy (μ-FTIR) is an appropriate method for identifying clay minerals in soil matrices. 2) Determine which minerals in our spectral library are applicable for studying boron (B) adsorption. Previous studies have found that amorphous $Fe(OH)_3$ and amorphous $Al(OH)_3$ are both suitable for B adsorption studies [1]. In past work we found a clear spectral differentiation between gibbsite that had been untreated with B and B treated could be detected [2]. These differences are due to specific adsorption of B onto the mineral surfaces. 3) Use a benchtop attenuated total reflectance-Fourier transformed infrared spectroscopy (ATR-FTIR) to examine the coordination of boron adsorption on magnesium hydroxide ($Mg(OH)_2$).

B has been identified as one of the major trace elements responsible for soil degradation in irrigated areas of the world [3]. Although B is an essential micronutrient for plants, it can also be toxic at concentrations greater than 1 mg L^{-1} [4]. In arid and semi-arid regions of the world, where soils are subject to high evapotranspiration rates and poor water quality, they can become enriched in B, becoming an important factor in leaving large areas in the landscape devoid of vegetation.

Boron biogeochemistry is a major factor in managing land reclamation in arid and semi-arid ecosystems. A key factor limiting progress in land management is understanding the processes involved in the retention and slow release of B from the soil inorganic and organic solid-phase. Combining μ-FTIR with ATR-FTIR and XRD, we aim to characterize the composition of the soil matrix and possibly the form and location of B in the soil matrix.

METHODS

Peds (intact pieces of soil) were collected from the Panoche soil series in Fresno County, CA. The Panoche soils are known to be high in B. Yellow and brown deposits were noted throughout the soil profile. The soil peds were air dried at 35^0C and impregnated with LR White high grade resin under a vacuum in order to retain soil aggregate structure. The resin was hardened by heating samples at 60^0C for 48 hours. The hardened samples were cut into thin sections (0.1-0.2 cm thick) using a diamond edged saw and polished to ensure a smooth surface. The thin sections were then analyzed using μ-FTIR on Beamline 1.4.3. The clay-sized fraction of this soils was also analyzed by XRD to determine clay mineralogy.

Minerals containing B, clay minerals and oxides were obtained for the spectral library. These minerals were analyzed by benchtop FTIR, μ-FTIR and XRD. This provided us with samples of known characteristics for comparison and were used to create a searchable library in Omnic 5.1.

Boron was also adsorbed onto brucite ($Mg(OH)_2$) at varying pH's. Samples of 0.3 g MgO were added to 50 mL polypropylene centrifuge tubes containing 25 mL's of 20 ppm B solution, and were shaken for 24 hrs. The suspension pH was adjusted to the desired levels with 1.0 M HCl or NaOH. The supernatant solutions were separated by centrifugation, filtered through a 0.1 mm filter and analyzed for B concentration by inductively couples plasma-atomic emission spectrometry (ICP-AES). The amount of B adsorbed was calculated as the difference between the total B added and the B that remained in the aqueous solution. The solid material remaining was air dried at room temperature and analyzed by ATR-FTIR and XRD.

RESULTS AND DISCUSSION

μ-FTIR seems to be an appropriate method for the qualitative identification of clay minerals. The spectral library of clay minerals created in Omnic 5.1 was able to correctly identify the clays (originally determined by XRD) in the Panoche soil we collected. The μ-FTIR was useful because we were able to determine the clay mineralogy of specific aggregates in our soil thick-sections. Figure 1 shows the results of a search on the soil matrix. The XRD work done on bulk samples of the Panoche soil gave the same results as the μ-FTIR. The μ-FTIR provides great advantages over common XRD procedures for determining the clay mineralogy which only considers homogenized bulk samples. The drawbacks to this method were that the signal from the hardening resin can interfere with the signal from the samples. Subtracting the resin signal did not remove the interference in all cases.

We found that many of the minerals commonly found in soils are inappropriate for studying B adsorption using FTIR. This is due to the fact that many clay minerals have adsorption bands in the same locations as B adsorption bands. The criteria for selecting minerals appropriate for this study was an absence of bands in the 1600-1150 cm^{-1} and the 1100-850 cm^{-1} region. Bands in the 1600-1150 cm^{-1} region make it difficult to detect trigonally coordinated B ($B(OH)_3$), and bands in the 1100-850 cm^{-1} region make it difficult to detect tetrahedrally coordinated B ($B(OH)_4^-$). Therefore, this criteria excludes most clay minerals from B adsorption studies using FTIR, since most clays have adsorption bands in the 1100-850 cm^{-1} region, due to the Si-O asymmetric stretching mode.

We found that $Mg(OH)_2$ may also be promising for B adsorption studies. Magnesium minerals have previously been identified as having appreciable boron-sorption capacities [5]. Since this discovery, no research has investigated this phenomenon in detail.

Samples of $Mg(OH)_2$ with 1046 mg B kg^{-1} sorbed were analyzed using ATR-FTIR. We could not identify any significant spectral differences between the B treated and untreated $Mg(OH)_2$. It is possible that the concentration is too low for IR detection or that B is not specifically adsorbing. Another explanation might be that the adsorption bands for trigonal B were masked by a broad adsorption band for carbonate at 1420 cm^{-1}. These solid phase carbonates may have formed in solution and adsorbed, or they could be carbonates formed at the surface of the mineral.

Figure 1 – Results of the Spectal Search for the Panoche Soil

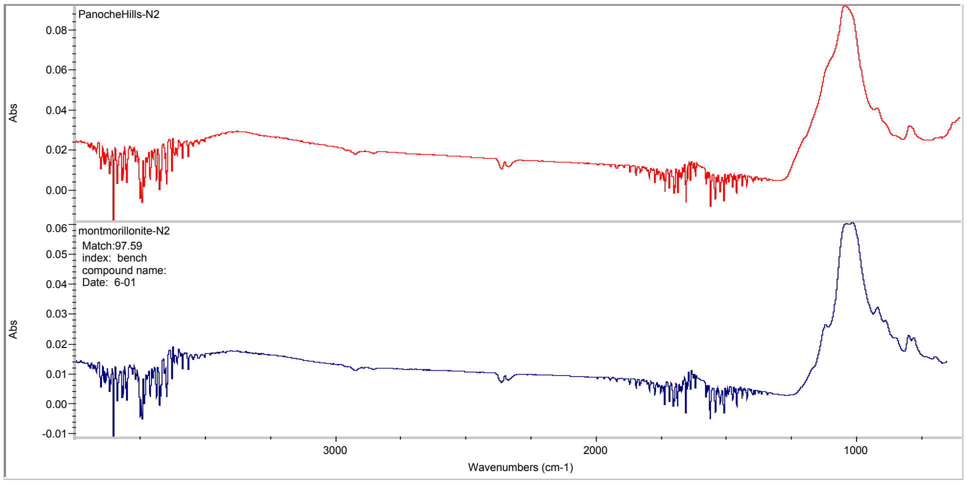

Figure 1 – The top IR spectrum is from the Panoche Soil Series and the bottom spectrum shows the library search results. This match shows that the Panoche soil is predominantly montmorillonite clay.

The μ-FTIR technique has many clear advantages for investigating chemical processes in natural microenvironments as exists in soils. Although our results over that past year were inconclusive, the development of a spectral library will greatly enhance the application of this technique. As an example, given the economic significance of B toxicity in many irrigated systems of the world, a greater understanding of the role of magnesium minerals in controlling the distribution of B in natural systems is crucial for predicting availability, potential toxicity problems, and is essential for evaluating how B rich soils should be managed.

LITERATURE CITED

[1]Chunming Su and Donald L. Suarez, "Coordination of adsorbed boron: An FTIR spectroscopic study," Environmental Science and Technology **29** (2), 302-311 (1995).

[2]P. Fox, H.E. Doner, and S. Pittiglio, "Micro-scale distibution of trace elements in a high boron soil from Kern County, California,", (2001).

[3]J. Hren and H. R. Feltz, "Effects of irrigation on the environment of selected areas of the Western United States and implications to world population growth and food production," Journal of Environmental Management **52** (4), 353-360 (1998).

[4]F. T. Bingham, A.W. Marsh, R. Branson et al., "Reclamation of salt-affected high boron soils in western Kern County," Hilgardia **41** (8), 195-211 (1972).

[5]J. D. Rhoades, R. D. Ingvalson, and J. T. Hatcher, "Adsorption of boron by ferromagnesian minerals and magnesium hydroxide," Soil Science Society of America Journal **34**, 938-941 (1970).

ACKNOWLEDGMENTS

We appreciate the assistance of Michael Martin of the ALS.

This work was supported by USDA regional research project CA-B*-ECO-5515-RR and USDA Hatch project CA-B*-ECO-6135-H

Principal investigator: Harvey Doner, Ecosystem Sciences Division – ESPM, University of California, Berkeley. Email: doner@nature.berkeley.edu. Telephone: 510-642-4148

Valence-state imaging of mineral micro-intergrowths

A.D.Smith[1], P.F.Schofield[2] and A.Scholl[3]

[1]CLRC Daresbury Laboratory, Daresbury, Warrington Cheshire, WA4 4AD United Kingdom
[2]Department of Mineralogy, The Natural History Museum, London, SW7 5BD United Kingdom
[3]Advanced Light Source, Ernest Orlando Lawrence Berkeley National Laboratory, University of California, Berkeley, California 94720, USA

INTRODUCTION

The crystal chemistry and textural relationships of minerals hold a vast amount of information relating to the formation, history and stability of natural materials. An understanding of the detailed crystal chemistry of minerals within rocks, meteorites, soils, sediments, mineral-fluid/biota interfaces etc. will ultimately develop both an understanding of the processes involved with their formation and also a knowledge of their properties, reactivity and stability within their current environment. The acquisition of such knowledge is, however, non-trivial, due in no small part to the vast array of textural relationships and mineral assemblages observed, combined with their polygenetic history.

Minerals generally comprise complex structures with large unit cells that contain complex and varied crystal chemistries. For example, the 3d transition metals impart a significant influence on mineral properties and behaviour, existing at major, minor and trace concentrations and also exhibiting multiple valence states. Knowledge of the valence state ratios of these metals within minerals and mineral assemblages is fundamental to the calculation of geochemical variables such as pressure, temperature and oxygen fugacity. The application of soft X-ray spectroscopy to mineralogical material has revealed that 2p($L_{2,3}$) spectra provide a sensitive fingerprint of the electronic states of 3d metals [1-4]. In bulk powdered samples much of the textural and microstructural information is lost, but the area-selectivity capability of X-ray Photo-Emission Electron Microscopy (XPEEM) provides the ability to obtain valence state information from mineral intergrowths with a submicron spatial resolution [5,6,7].

RESULTS

Sulphide Intergrowths

Pentlandite, $(Fe,Ni)_9S_8$, is the primary sulphide ore of Ni and usually occurs intergrown with the iron sulphide pyrrhotite, FeS. Figure 1 shows data obtained using the PEEM2 beamline at ALS and reveals the high quality of imaging and XAS data that can be obtained from XPEEM. The left hand image has an estimated field of view < 20μm and was taken at 715.0eV, the main feature of the FeS pyrrhotite Fe $L_{2,3}$ spectrum. It thus shows the distribution of Fe in the chemical state equivalent to that of Fe in pyrrhotite. The light grey areas represent Fe from pyrrhotite, whereas the dark grey regions represent the Fe in pentlandite. The Fe $L_{2,3}$ spectrum below the image has been collected from the full image area. XPEEM allows an area selectivity such that an Fe $L_{2,3}$ spectrum can be obtained from any area of the image, thus providing a spatial resolution in the order of 0.1μm. The right hand image, with an estimated field of view < 40μm, is taken at 864.5eV the main feature of the $(Fe,Ni)_9S_8$ pentlandite Ni $L_{2,3}$ spectrum and the Ni $L_{2,3}$ spectrum from the whole image is below this image. Close investigation has shown banding of nickel and iron, with possible variations in the chemical state of the iron, in the ‘feathers’ of the pentlandite on a sub 200nm scale.

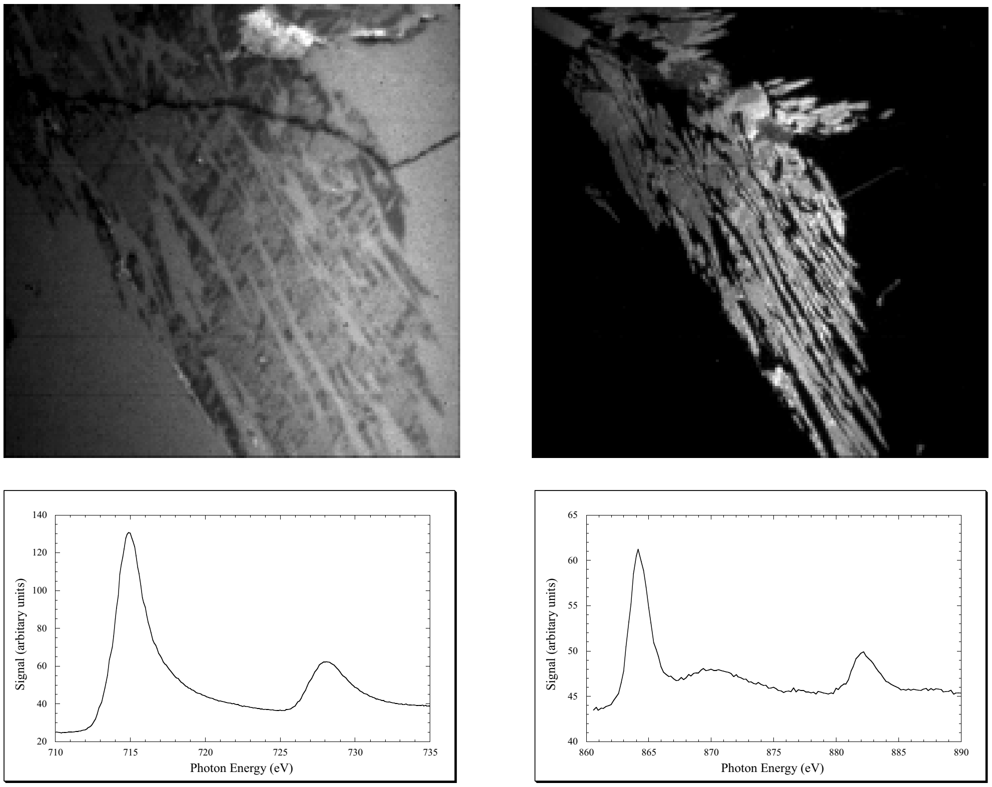

Figure 1. PEEM2 images from a pentlandite/pyrrhotite intergrowth. The left hand image is taken at 715.0eV – the main feature of the Fe L_{23} spectrum (below), and the right hand image was recorded at 864.5eV – the principal feature of the Ni L_{23} spectrum (below).

Hydrothermal Vent Sediments

Sulphide-to-oxide alteration behaviour in sea-floor hydrothermal vent samples recovered from the North Atlantic may potentially be observed from metal and sulphur valence information on a microscopic length scale. Mn^{2+}/ Mn^{3+}/ Mn^{4+} ratios as well as Fe^{3+}/Fe^{2+} are likely to be related to the extent of sulphate-reducing bacteria active at different horizons in these recent sea-floor hydrothermal deposits. Little is known about the micro-ecology in which these bacteria live, however it is thought that they are able to substantially modify their environment due to large differences observed in the redox conditions of various minerals contained in different strata of sea floor cores. Figure 2 shows iron, copper and oxygen chemical state images in a sample taken from the sediment around an active hydrothermal vent on the mid-Atlantic ridge. The unconsolidated sediment has been embedded in epoxy resin, sliced and polished but still provides excellent images and $L_{2,3}$ spectra.

The PEEM2 images show clear growth features that may reflect differing environments, oxidizing conditions and micro-ecologies. The top images show alternating Cu and Fe growth rings on the submicron scale indicating a low oxygen environment. The lower images show a submicron thick, copper sulphide precipitate that has grown around an iron sulphide grain. This ring represents both a different source fluid and a more reduced environment to that of the bulk Fe-oxides present in the image.

ACKNOWLEDGEMENTS

This work was funded by the UK ENVIROSYNCH project and the authors are grateful to Professor C.M.B. Henderson and Dr J.F.W. Mosselmans for the provision and management of this project. Beamtime at ALS was awarded under project code ALS-548. The assistance of Hendrik Ohldag and Andrew Doran on the PEEM2 beamline is also greatly appreciated.

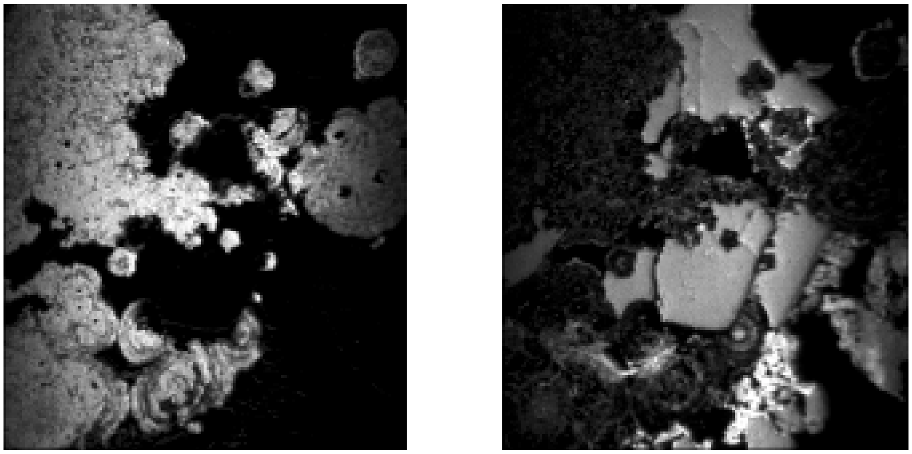

Figure 2. PEEM2 chemical state images from a sediment associated with a mid-Atlantic ridge hydrothermal vent. The top images are Cu (left) & Fe (right) and have a field of view of <30μm and reveal clear botryoidal textures or growth features that may be related to bacterial micro-ecological cycles. The lower images are Fe (left), Cu (middle) & O (right) and have a field of view of <20μm. The Cu 'ring' appears to be a sulphide precipitate with a thickness of about 0.5<30μm that has grown around an Fe sulphide grain. The majority of the Fe phases in these images are clearly oxidized

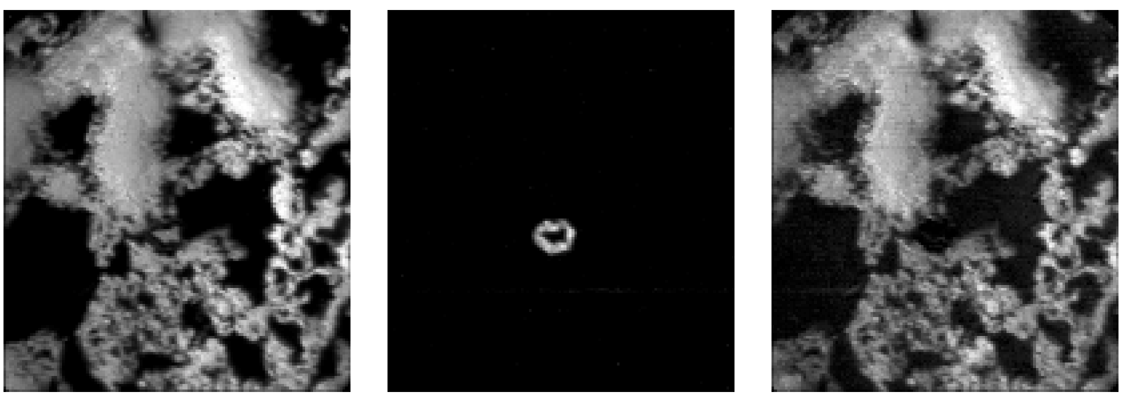

REFERENCES

[1] Cressey G. et al. (1993) Physics and Chemistry of Minerals 20 pp111-119
[2] Henderson C.M.B. et al. (1995) Radiation Physics and Chemistry 45 pp459-481
[3] Schofield P.F. et al. (1995) Journal of Synchrotron Radiation 2 pp93-98
[4] van der Laan G. and Kirkman I.W. (1992) Journal of Physics: Condensed Matter 4 pp4189-4202
[5] Smith A.D. et al. (1998) Journal of Synchrotron Radiation 5 pp1108-1110
[6] Cressey G. et al. (1998) 17th General Meeting, International Mineralogical Association, A128
[7] Smith A.D. et al. (1999) ALS Compendium 1997/8

Principal investigator: A.D. Smith, CLRC, Daresbury Laboratory. Telephone: 44-1925-603314.
Email: a.d.smith@dl.ac.uk.